7 SCIENTIFIC HIGHLIGHT OF THE MONTH: "Electronic Excitations in Nanostructures: An Empirical Pseudopotential based Approach

---

Electronic Excitations in Nanostructures: An Empirical Pseudopotential based Approach

Gabriel Bester

Max-Planck Institut für Festkörperforschung, Heisenbergstr. 1, D-70569 Stuttgart

Abstract

Physics at the nanoscale has emerged as a field where discoveries of fundamental physical effects lead to a greater understanding of the solid state. This area of research is additionally driven by high hopes for technological relevance and a high pace of experimental achievements in fabrication and characterization has been witnessed in the last decade. From the side of theoretical modeling —so successful in solid state physics in general, since the emergence of density functional theory— we must acknowledge a weak connection to state of the art experimental achievements in the realm of nanostructures. The cause for this partial disconnect resides in the difficulty of the matter. Nanostructures being small in size but large in the number of atoms constituting them, and the relevant observables being accessible only through proper treatment of excitations. The large number of atoms and the need for excited sate properties makes this a challenging task for theory and modeling.

In this contribution we will outline the framework, based on empirical pseudopotentials and configuration interaction, to obtain quantitative predictions of the excited state properties of semiconductor nanostructures using their experimental sizes, compositions and shapes. The methodology can be used to describe colloidal nanostructure of few hundred atoms all the way to epitaxial structures requiring millions of atoms. The aim is to fill the size gap existing between *ab initio* approaches and continuum descriptions. Based on the pseudopotential idea and the developments of empirical pseudopotentials for bulk materials in the early 60's, the method has evolved into a powerful tool where the pseudopotential construction has lost some of its empirical character and is now based on modern density functional theory. We will present the construction of these potentials and the way the ensuing wave functions are used in a subsequent configuration interaction treatment of the excitation. We will illustrate the available capabilities by recent applications of the methodology to unveil new effects in the optics of nanostructures, quantum entanglement and wave function imaging.

1 Introduction

The new class of materials formed by semiconductor nanostructures has a **large and mostly unexplored ensemble of possible applications**. For instance, colloidal semiconductor nanostructures are used today in biology and medicine as light-emitting markers that remain inert in the bio-environment. They can help to resolve structures and processes within the cells and can tag body substances. In the area of *classical* information science and technology they have a strong potential for providing efficient tunable light sources and light detectors. In general, optoelectronics could profit from the developments of semiconductor nanostructures. Following a rather long-term goal, in the area of *quantum* information science and technology (towards the realization of single-photon sources, sources of entangled photons, or quantum gates and register all the way to a quantum computer), the use of quantum dots is one of the most promising concepts and is lead by a world-wide effort.

As a general remark one could note that the field of nanostructure science is driven by a high pace of experimental achievements. Experimentalists are now able to grow nanostructures of high quality from **diverse semiconductor materials** [1] with the ability to dope them [2–9]. The area of characterization reveals increasingly **complex behavior**, including the appearance of high-energy excited excitons [10], charged excitons [11], multi excitons [12], exchange-induced splittings [13], Coulomb blockade in addition spectra [14, 15], spin blockade [16], quantum entanglement [17], enhancement of electron-hole exchange interactions [18], carrier relaxation and multiplication via Auger processes [19], and the observation of quasiparticle wave functions through magnetotunneling experiments [20] and scanning tunneling microscopy [3, 21, 22].

Nanostructures have therefore potential for applications, they cover a diverse set of materials and structures, and they revel complex behavior revealed through a growing number of characterization methods leading to interesting and fundamental physical effects. At this point we should emphasize that the nanometer-scale that is the focus of *nanotechnology* describes structures with dimensions of several nanometers up to hundreds of nanometers. While these structures are "small" they do comprise thousands up to hundred thousands of atoms. In short: **nanometer-scale means thousands of atoms.** Smaller structures are referred to as *clusters* and are often of poor quality, showing broad size and shape distributions, poor surface passivations and optical properties. We must conclude that to address the relevant size regime and the relevant physical observables, we need to be able to address a large number of atoms, including excitations and many-body effects.

The current status of theoretical capabilities for describing the electronic and optical properties of semiconductor nanostructures is as follows. Optical properties can be calculated from atomistic **first-principles** (Quantum Monte Carlo, time-dependent density functional theory, GW and Bethe Salpeter,...) for nanosystems containing few to 200 atoms (depending on the level of approximation). Pending a revolutionary change in our current approach to many body physics, extensions of these approaches are unlikely to be able to address the size regime described above. However, the development of first principles *ab initio* methods is important since it gives many insights into the physics in strong confinement and can often be used as benchmark. **Continuum models** such as effective-mass and $\mathbf{k} \cdot \mathbf{p}$ [23], can handle macroscopic nano systems but fail to address nanostructure where atomistic effects become important [24–26]. **Empirical**

Tight binding models [27, 28] can presently deal with millions of atoms but lack atomistic wave functions (since the Hamiltonian is directly parametrized) which constitute the essence of the many-body problem.

In this contribution we will present the empirical- and semiempirical-pseudopotential methods that can be used in conjunction with configuration interaction to obtain many-body wave functions of structures with millions of atoms. More than the bare empirical pseudopotential construction, we will survey the different steps that can lead to the calculation of the observables relevant to modern experiments, using the experimental nanostructure geometry. We will conclude by presenting three recent applications of the developed formalism.

2   Method

A summary of the methodology is given in Figure 1 in the form of a flowchart summarizing the different components of our current approach. Figure 1 is divided into three logical segments, labelled as *Ground State*, *Excitations* and *Observables*, feeding into each other. The calculation of the ground state requires the input of the geometry and relaxation of the atomic positions to minimize strain. The generation of empirical pseudopotentials is the prerequisite for the construction of the total crystal potential that is subsequently used in the Schrödinger equation. The ensuing eigenfunctions are fed into a configuration interaction treatment to obtain excitations. Finally, from the many-body wave functions, observables can be obtained through the use of post processor tools. These different components will be introduced by using Figure 1 as the thread of the discussion.

2.1   Input geometry and geometry relaxation

In the first step of the flowchart in Fig. 1, *Input Geometry*, we construct a supercell containing the nanostructure. The shape, size and composition are taken as initial input from experiments and the atoms are placed, at first, on a regular grid representing an initial guess for the final atomic positions to be obtained in the next step. The atoms within the supercell are then allowed to relax in oder to minimize the strain energy. In most cases, the system of interest is too large to be handled by standard density functional theory and we make use of a classical atomistic force field model [29–31], the Valence Force Field (VFF) method, including bond bending, bond stretching and bond bending-bond stretching interactions:

$$
\begin{aligned}
E_{VFF} &= \sum_i \sum_j^{nn_i} \frac{3}{8} [\alpha_{ij}^{(1)} \Delta d_{ij}^2 + \alpha_{ij}^{(2)} \Delta d_{ij}^3] + \sum_i \sum_{k>j}^{nn_i} \frac{3\beta_{jik}}{8d_{ij}^0 d_{ik}^0} [(\mathbf{R}_j - \mathbf{R}_i) \cdot (\mathbf{R}_k - \mathbf{R}_i) \\
&- cos\theta_{jik}^0 d_{ij}^0 d_{ik}^0]^2 + \sum_i \sum_{k>j}^{nn_i} \frac{3\sigma_{ijk}}{d_{ik}^0} \Delta d_{ij}[(\mathbf{R}_j - \mathbf{R}_i) \cdot (\mathbf{R}_k - \mathbf{R}_i) - cos\theta_{jik}^0 d_{ij}^0 d_{ik}^0] \quad , \ (1)
\end{aligned}
$$

where $\Delta d_{ij}^2 = \left[[(R_i - R_j)^2 - d_{ij}^{0\,2}]/d_{ij}^0 \right]^2$. Here $\mathbf{R}_i$ is the coordinate of atom i and d_{ij}^0 is the ideal (unrelaxed) bond distance between the atoms i and j. Also, θ_{jik}^0 is the ideal (unrelaxed) angle of the bond angle $j - i - k$. The $\sum^{nn_i}$ denotes summation over the nearest neighbors of atom i. The bond stretching, bond angle bending, and bond-length/bond-angle interaction coefficients
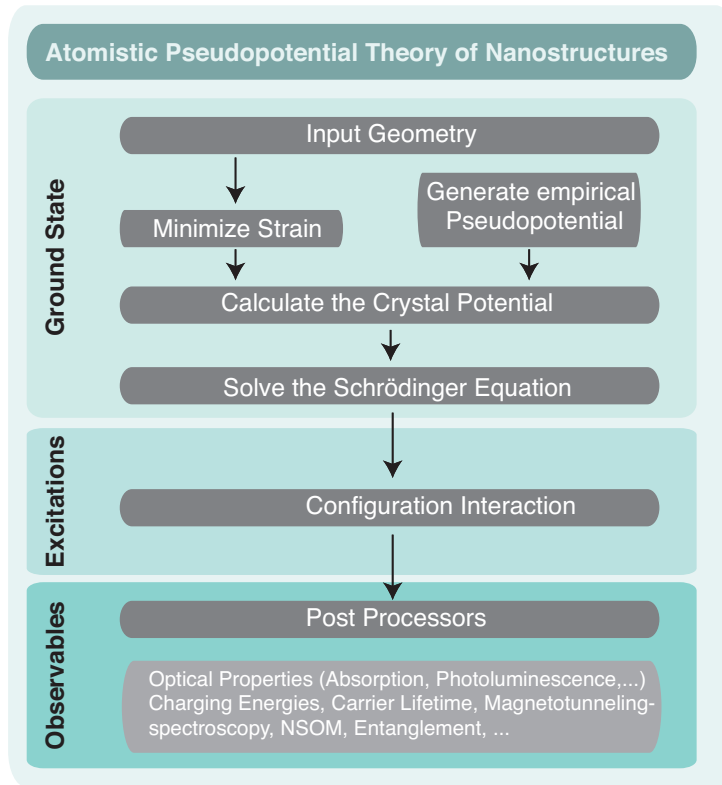
Figure 1: Flowchart of the methodology underlying the atomistic calculation of various observables for semiconductor nanostructures. The flowchart is divided into three logical sections: Ground State, Excitations (many-body part), and Observables. The different computational parts are described in the text.

$\alpha_{ij}^{(1)}(\equiv \alpha)$, β_{jik}, σ_{jik} are directly related to the elastic constants in a pure zincblende structure [32]. The second-order bond stretching coefficient $\alpha^{(2)}$ is related to the pressure derivative of the Young's modulus by $\frac{dB}{dP}$, where $B = (C_{11} + 2C_{12})/3$ is the Young's modulus.

An atomic force field is similar to continuum elasticity approaches [30] in that both methods are based on the elastic constants, $\{C_{ij}\}$, of the underlying bulk materials. However, atomistic approaches are superior to continuum methods in two ways, (a) they can contain anharmonic effects, and (b) they capture the correct point group symmetry. The calculation of the energy and forces from expressions such as Eq. (1) can be performed within seconds for millions of atoms, allowing for a manageable strain minimization of large nanostructure.

2.2 Pseudopotentials

It is advantageous to split the electrons into core and valence electrons. The valence electrons occupy the outer shells and interact with the potentials of the neighboring atoms. They are responsible for the interatomic binding, in contrast to the atom-localized core electrons. In the *frozen core* approximation, the core electrons are assumed to be unperturbed by their environment and the Schrödinger equation has to be solved only for the valence electrons. The assumption that the core electrons are independent of their surroundings is poorly fulfilled [33], but the change in energy vanishes in the first order of density change [33,34] making this approximation practical. The frozen core approximation is the founding assumption of pseudopotentials.

The Pauli principle requires from the valence wave functions to be orthogonal to the core wave functions leading to valence wave functions that are fast oscillating in the core region with high kinetic energy. This behavior can be pictured with a virtual repulsive potential at the ion cores. It turns out that this repulsion is nearly perfectly compensated by the attractive core potential, both effects leading to a weak effective potential acting on the valence electrons[1].

Following the formulation of Phillips and Kleinman [35] the formal justification of pseudopotentials can be given as follows. $|\psi\rangle$ represents the valence wave functions and $\{|\chi_n\rangle\}$ the core wave functions with eigenvalues $\{E_n\}$. The aim is to construct a node-free pseudo–wave function $|\phi\rangle$. Initially, we assume:

$$|\psi\rangle = |\phi\rangle + \sum_n c_n|\chi_n\rangle \quad . \tag{2}$$

From the orthonormality relation we obtain:

$$\langle\chi_n|\psi\rangle = 0 = \langle\chi_n|\phi\rangle + c_n \longrightarrow c_n = -\langle\chi_n|\phi\rangle \tag{3}$$

and

$$|\psi\rangle = |\phi\rangle - \sum_n |\chi_n\rangle\langle\chi_n|\phi\rangle \quad . \tag{4}$$

This expression for the valence wave functions is used in the Schrödinger equation $\widehat{H}|\psi\rangle = E|\psi\rangle$:

$$\widehat{H}|\psi\rangle = \widehat{H}|\phi\rangle - \sum_n \widehat{H}|\chi_n\rangle\langle\chi_n|\phi\rangle = \widehat{H}|\phi\rangle - \sum_n E_n|\chi_n\rangle\langle\chi_n|\phi\rangle = E|\psi\rangle \tag{5}$$

$$= E|\phi\rangle - \sum_n E|\chi_n\rangle\langle\chi_n|\phi\rangle \quad , \tag{6}$$

and the terms are rearranged:

$$\widehat{H}|\phi\rangle + \sum_n (E - E_n)|\chi_n\rangle\langle\chi_n|\phi\rangle = E|\phi\rangle \quad . \tag{7}$$

The node-free pseudo–wave functions fulfill a Schrödinger equation with an additional energy dependent non-local pseudopotential $\widehat{V}_{nl}$:

$$\widehat{T}|\phi\rangle + \left\{\widehat{V} + \underbrace{\sum_n (E - E_n)|\chi_n\rangle\langle\chi_n|}_{\widehat{V}_{nl}}\right\}|\phi\rangle = E|\phi\rangle \quad , \tag{8}$$

where $\widehat{H}$ has been split into kinetic $\widehat{T}$ and potential $\widehat{V}$ terms. The expression in curly brackets is the pseudopotential, which is made of a positive attractive part $\widehat{V}$ and a negative repulsive part $\widehat{V}_{nl}$. The eigenvalues of the Schrödinger equation for the real– and the pseudopotential are identical since Eq. (7) can be rewritten as:

$$\langle\psi|H|\phi\rangle + \sum_n (E - E_n)\langle\psi|\chi_n\rangle\langle\chi_n|\phi\rangle = E\langle\psi|\phi\rangle \quad , \tag{9}$$

and the core and valence states must be orthogonal: $\langle\psi|\chi_n\rangle = 0$.

The pseudopotential at this point is not necessarily soft since $\widehat{V}_{nl}$ includes core states but it is not unique, since $(E - E_n)$ can be arbitrarily replaced. This non-uniqueness will be used to generate

---

[1]This compensation is only effective when electrons with the angular momentum of the valence electrons are present in the core. A lack of thereof lead to strong (or hard) pseudopotentials.

soft pseudopotentials. The pseudopotential is also non-local since the projector $|\chi_n\rangle\langle\chi_n|$ applied on the pseudo-wave functions yields a volume integration $|\chi_n\rangle\langle\chi_n|\phi\rangle$. The pseudopotential also depends on energy and acts mainly in the core region.

At this point where we have established the partial cancellation of attractive and repulsive parts of the potential [35, 36] and given a formal derivation for weak pseudopotentials, there are two possible routes.

- The construction of ionic pseudopotentials where the interaction of valence electrons is explicitly taken into account. This route has been very successful, especially when *ab initio* calculations for the atom have been used to construct transferable and accurate pseudopotentials. One of the requirements for such pseudopotentials is to deliver pseudo-wave functions identical to the real all-electron wave functions outside of a certain cut-off radius. This guarantees to obtain accurate binding properties. There are several implementations of ionic pseudopotentials starting with norm-conserving pseudopotentials where the generalized eigenvalue problem of Eq. (8) (the pseudo-wave function are not orthogonal, Eq. (4)) is transformed to a standard eigenvalue problem where the pseudo-eigenfunctions satisfy the orthonormality condition. The norm conservation guarantees that the important scattering properties only change in second order with a change in energy [37–40] which is the key ingredient for the good transferability of these potentials. The most common construction procedures are due to Vanderbilt [41], Hamann, Schlüter and Chiang [40,42] , Troullier and Martins [43], and von Kerker [44]. Another type of ionic pseudopotentials are *ultrasoft pseudopotentials (US)* [45,46] where the norm-conservation is not explicitly required for the pseudo valence wave functions at the expense of introducing an auxiliary function acting at the ionic cores. Yet another type of ionic pseudopotentials are used in the *projector augmented waves (PAW)* [47] method. Like for ultrasoft pseudopotentials, projectors and auxiliary functions are introduced but the all-electron wave function is kept. This involves in the calculation of the integrals smooth functions extending outside the core region and functions localized inside of muffin-tin spheres.

- The construction of total pseudopotentials that include the interaction of not only the core electrons but of all electrons. This is the route taken in the construction of empirical and semiempirical pseudopotentials, as described in the next section.

2.3   Empirical pseudopotentials and their construction

The empirical pseudopotential method (EPM) (see Ref. [48] and references therein for a more detailed review of the method and a historical introduction) involves a fit of the reciprocal space pseudopotential $V(\mathbf{G})$ to experimentally known quantities, such as certain points of the band structure. The first assumption is that the self-consistent effective pseudopotential of the crystal (we use capital V for crystal potentials and lower-case v for atomic potentials) can be written as a sum of atom-centered pseudopotentials:

$$V(\mathbf{r}) \quad = \quad \sum_{\alpha,j,n} v_\alpha(\mathbf{r} - \mathbf{R}_n - \mathbf{r}_{\alpha,j}) \quad , \tag{10}$$

where n is the index for the primitive unit cells and $\mathbf{R}_n$ the corresponding lattice vector. α stands for the atom type and j is the atom index. $\mathbf{r}_{\alpha,j}$ is therefore the basis vector for the atom

j of type α. Simplifying, at first, to a crystal with only one type of atoms (e.g. Si), v, we can write the potential in reciprocal space as

$$V(\mathbf{r}) \;=\; \sum_{\mathbf{G}} v(\mathbf{G}) S(\mathbf{G}) e^{i\mathbf{Gr}} \quad , \tag{11}$$

with the structure factor

$$S(\mathbf{G}) = \frac{1}{n} \sum_{j} e^{-i\mathbf{Gr_j}} \quad , \tag{12}$$

where n is the number of basis atoms. The structure factor only depends on the geometry. The potential $v(\mathbf{G})$, also called the form factor, is treated in the EPM as disposable parameter.

To illustrate the practical implications of this formalism, we take the example of Si in the diamond structure. The lattice vectors in real and reciprocal space are given by $\mathbf{A}$ and $\mathbf{B}$ and the vectors of the two basis atoms by $\mathbf{r}$ and $-\mathbf{r}$:

$$\mathbf{A} = \frac{a_0}{2} \begin{pmatrix} 1 & 1 & 0 \\ 0 & 1 & 1 \\ 1 & 0 & 1 \end{pmatrix} \quad , \quad \mathbf{B} = \frac{2\pi}{a_0} \begin{pmatrix} 1 & 1 & -1 \\ -1 & 1 & 1 \\ 1 & -1 & 1 \end{pmatrix} \quad , \quad \mathbf{r} = \frac{a_0}{8} \begin{pmatrix} 1 \\ 1 \\ 1 \end{pmatrix} \quad . \tag{13}$$

In this case, the structure factor from Eq. (12) simplifies to

$$S(\mathbf{G}) = \cos(\mathbf{G} \cdot \mathbf{r}) \quad . \tag{14}$$

A few reciprocal lattice vectors sorted according to their length are given in Table 1. According

Table 1: Reciprocal lattice vectors $\mathbf{G}$ with smallest length in diamond structure with lattice constant a_0.

$\frac{a_0}{2\pi}\mathbf{G}$	$\left(\frac{a_0}{2\pi}\mathbf{G}\right)^2$	$\mathbf{G} \cdot \mathbf{r}$
000	0	0
{111}	3	$3\pi/4$
{200}	4	$\pi/2$
{220}	8	π
{311}	11	$5\pi/4$

to Eq. (14) and Table 1 the structure factor for $\mathbf{G}^2 = 4(2\pi/a_0)^2$ vanishes. It turns out that for Si and most conventional group IV, and III-V semiconductors the potential $\mathbf{G}$ becomes week for reciprocal vectors larger than $\mathbf{G}^2 = 11(2\pi/a_0)^2$, so that truncating the expansion at this point turns out to be a reasonable approximation. The $\mathbf{G}=0$ component of the form factor simply gives the averaged potential and shifts the band structure rigidly along the energy axis. If we further assume that $v(\mathbf{r})$ is spherically symmetric the form factor takes the form $v(G)$ and only three different form factors remain. These three factors, v_{111}, v_{220} and v_{311} are used as adjustable parameters to reproduce experimental results, such as the band structure. Early applications of the method were done for Si and Ge [49, 50] and soon extended to fourteen different semiconductors [51] with surprisingly accurate results, considering the limited input. The band structure of most semiconductors can be fitted to high accuracy using this procedure

giving us the hint that a local potential $V(r)$ can be used as a mean field to describe the complex many-body electronic interactions in the crystal.

The application of this idea to calculate the electronic properties of nanostructures requires a continuous form of $v(G)$ since the few discrete points, v_{111}, v_{220} and v_{311}, fail to address a large structure with a dense mesh of $\mathbf{G}$ vectors. The continuous empirical pseudopotential can be represented, for instance, by a function with 4 parameters a_1,a_2,a_3,a_4 [52] or by a sum of N Gaussians with parameters a_i, c_i, b_i [53]:

$$v^{\text{EPM}}(q) = \frac{a_1(q^2 - a_2)}{a_3 e^{a_4 q^2} - 1} \quad \text{or} \quad v^{\text{EPM}}(q) = \sum_{i=1}^{N} a_i e^{-c_i(q-b_i)^2} \quad . \tag{15}$$

From the empirical atomic pseudopotentials $v(q)$ we construct the *bulk* crystal empirical pseudopotential $V(\mathbf{r})$ from the sum given in Eq. (10). We solve the Schrödinger equation

$$\widehat{H}\psi_i(\mathbf{r}) = \{-\frac{\nabla^2}{2} + V_{loc}^{\text{EPM}}(\mathbf{r}) + \widehat{V}_{\text{SO}}\}\psi_i(\mathbf{r}) = \varepsilon_i \, \psi_i(\mathbf{r}) \quad , \tag{16}$$

using a basis set of plane waves with a low energy cut-off (e.g., 4.5 Ry for Si in Ref. [52]). At this point, the parameters from Eqs. (15) are fitted to reproduce known experimental quantities such as the bulk band structure at high symmetry points, the effective masses for different bands at different k-points and along different reciprocal space directions, the deformation potentials, the surface work function [32,52,53]. The nonlocal spin-orbit interaction can be written as [54,55]

$$\widehat{V}_{SO} = \sum_{i\alpha} \hat{V}_\alpha^{SO}(R_i) = \sum_{i\alpha} \sum_{lm} V_{l,\alpha}^{SO}(r - R_i)|P_{lm}(\mathbf{R}_i)\rangle \mathbf{L} \cdot \mathbf{S} \langle P_{lm}(\mathbf{R}_i)| \quad , \tag{17}$$

where $|P_{lm}(\mathbf{R}_i)\rangle$ is a projector of angular momentum lm centered at the atomic position $\mathbf{R}_i$, $\mathbf{L}$ is the spatial angular momentum operator, $\mathbf{S}$ is the spin operator with components given by Pauli matrices, and $V_{l,\alpha}^{SO}(r)$ is a potential describing the spin-orbit interaction. The functional form of $V_{l,\alpha}^{SO}(r)$ was set to a Gaussian and only the effect of p states ($l=1$) was included in most recent works [31,56]. In practice this approach leads to a single spin-orbit parameter for each atom type α.

There have been several modifications to the approach from Eq. (16). The most prominent ones are *(i) The strain dependence of the potential* through the local hydrostatic strain $\text{Tr}(\epsilon)$ [31]:

$$v_\alpha^{\text{EPM}}(r; \epsilon) = v_\alpha^{\text{EPM}}(r)[1 + \gamma_\alpha \text{Tr}(\epsilon)] \quad , \tag{18}$$

where γ_α is a fitting parameter. The explicit strain dependence of the potential helps to capture effects that would enter the picture only through a self-consistent charge rearrangement in response to compression or expansion, which is absent in the conventional EPM framework. More sophisticated strain dependences have been introduced for nitride pseudopotentials [57].

(ii) The rescaling of the kinetic energy. In Eq. (16), the kinetic energy of the electrons has been scaled [31,56] by a fitting parameter β: $-\beta\nabla^2/2$. This procedure can be seen as the attempt to correct for the lack of non-locality in the potential. The introduction of β enables to fit both the band gap and the effective masses with the same set of few parameters.

(iii) The environment dependence of the potential. If the EPM is used to describe common-anion or common-cation alloys of semiconductors the question of environment dependence needs to

47
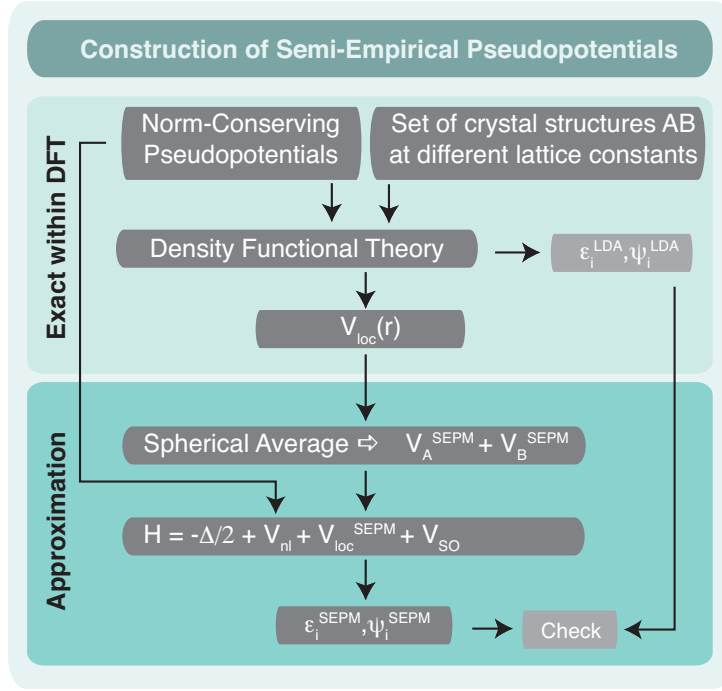
Figure 2: Flowchart describing the steps necessary to generate a semi-empirical pseudopotential (SEPM).

be addressed. For a common anion semiconductor (e.g., $In_xGa_{1-x}As$) each anion is surrounded by n cations of type 1 (e.g., Ga) and $4 - n$ cations of type 2 (e.g. In). The pseudopotentials are always constructed from independent binaries (e.g, InAs and GaAs) so that there are two, likely different, pseudopotentials for the same anion (e.g. As). This is legitimate since the pseudopotential describes not only the bare atom but also the interaction with its neighbors. However, the potentials should remain similar enough to guarantee some degree of transferability. The simplest expression for an As atom surrounded by n Ga and $(4-n)$ In atoms, is a weighted sum of the type:

$$v_{As}(n\text{Ga}, (4-n)\text{In}) = \frac{1}{4}\left(n\,v_{As}^{GaAs} + (4-n)\,v_{As}^{InAs}\right) \quad , \tag{19}$$

where $v_{As}^{InAs(GaAs)}$ represents the As pseudopotentials derived from InAs (GaAs). With this approximation, the parameters in Eqs. (15,17,18) can be slightly modified to correctly reproduce *alloy* properties, such as band gap bowing [53, 58].

2.4 Semi-Empirical Pseudopotentials and their Construction

The EPM framework we described uses a fully local description of the potential, besides the spin-orbit term in Eq. (17). It was soon recognized [59] that this approach can be improved by using non-local potentials. The non-locality is introduced by making the potential dependent on the angular momentum of the electron. It can therefore account for the different behavior of a 2s and a 2p electron in oxygen, for instance. The l-dependent potential v_l can be written as

$$\widehat{V}_{nl}(\mathbf{r}) = \sum_{\mathbf{R}_i} \widehat{v}_{nl}(\mathbf{r} - \mathbf{R}_i) = \sum_{\mathbf{R}_i}\sum_{lm} |P_{lm}(\mathbf{R}_i)\rangle v_l(|\mathbf{r} - \mathbf{R}_i|)\langle P_{lm}(\mathbf{R}_i)| \quad , \tag{20}$$

where $\mathbf{R}_i$ are the atomic positions and $|P_{lm}(\mathbf{R}_i)\rangle$ are projectors of angular momentum lm. In practice $\widehat{v}_{nl}(r)$ is assumed zero outside a cut-off radius r_{cut} typically around the interatomic

distance [53, 60]. This procedure is perfectly equivalent to the one used in the community of *ab-initio* ionic pseudopotentials. There, *l*-dependent ionic pseudopotentials are generated based on all-electron density functional theory (DFT) calculations [40–44]. This similarity in the formalism can be used to connect the total semi-empirical pseudopotentials with the ionic *ab-initio* pseudopotentials.

We will describe the necessary steps to the construction of the ionic semiempirical pseudopotentials following the flowchart of Fig. 2. From DFT in the local density approximation (LDA) the screened local (self-consistent) potential for a set of different crystal structures (zincblende, wurtzite, B2, ...) at different lattice constants is calculated. The norm-conserving *ab initio* ionic pseudopotentials required for the DFT calculations can be obtained from available databases or constructed with ease. The relevant output of the DFT calculation is the screened local effective potential, usually given in real space $V_{\text{loc}}(\mathbf{r})$. Fourier transformed to $\mathbf{G}$ space:

$$V_{\text{loc}}(\mathbf{G}) = \frac{1}{\Omega} \int_{\Omega} V_{\text{loc}}(\mathbf{r}) e^{i\mathbf{r}\mathbf{G}} \, d^3\mathbf{r} \quad . \tag{21}$$

For the local real space potential we make the Ansatz:

$$V_{\text{loc}}(\mathbf{r}) = \sum_{n} v_{\text{anion}}(\mathbf{r} - \mathbf{R}_n + \mathbf{r_0}) + v_{\text{cation}}(\mathbf{r} - \mathbf{R}_n - \mathbf{r_0}) \quad , \tag{22}$$

with the Fourier transform

$$V_{\text{loc}}(\mathbf{G}) = \frac{1}{\Omega} \int_{\Omega} v_{\text{anion}}(\mathbf{r}') e^{i\mathbf{G}(\mathbf{r}'-\mathbf{r}_0)} + v_{\text{cation}}(\mathbf{r}') e^{i\mathbf{G}(\mathbf{r}'+\mathbf{r}_0)} \, d\mathbf{r}' \tag{23}$$

$$= \frac{\cos(\mathbf{r}_0\mathbf{G})}{\Omega} v_+(\mathbf{G}) - i\frac{\sin(\mathbf{r}_0\mathbf{G})}{\Omega} v_-(\mathbf{G}) \quad , \tag{24}$$

using the short form

$$v_+(\mathbf{G}) = v_{\text{anion}}(\mathbf{G}) + v_{\text{cation}}(\mathbf{G}) \quad , \quad v_-(\mathbf{G}) = v_{\text{anion}}(\mathbf{G}) - v_{\text{cation}}(\mathbf{G}) \quad . \tag{25}$$

In Eq.(22) we separated the real space potential into an anion-centered and a cation-centered contribution, this represents the case of a binary system, e.g. a III-V semiconductor such as GaAs. If $v_{\text{cation/anion}}(\mathbf{r})$ is assumed to have inversion symmetry then $v_+(\mathbf{G})$ and $v_-(\mathbf{G})$ are real and we can write:

$$v_+(\mathbf{G}) = \frac{\Omega}{\cos(\mathbf{r}_0\mathbf{G})} \, \Re\{V_{\text{loc}}(\mathbf{G})\} \quad , \quad v_-(\mathbf{G}) = -\frac{\Omega}{\sin(\mathbf{r}_0\mathbf{G})} \, \Im\{V_{\text{loc}}(\mathbf{G})\} \quad . \tag{26}$$

It is possible to obtain $v_{\text{anion}}(\mathbf{G})$ and $v_{\text{cation}}(\mathbf{G})$ exactly. However, v_{anion} and v_{cation} are very well represented by their spherically averaged counterparts: $v_{\text{anion}}(|\mathbf{G}|)$ and $v_{\text{cation}}(|\mathbf{G}|)$ and we make use of this simplification, which represents a pivotal approximation. The DFT results for $v_+(|\mathbf{G}|)$ in GaAs calculated for the crystal structures zincblende and B2, each of them at the two lattice constants 10.658 a.u. and 11.452 a.u. are given as black dots in Figure 3. The inset (Fig 3(b)) is a magnification of the area indicated by black arrows. It can be seen that the discrete points mostly lie on a smooth curve. The fit through the points in Fig. 3 was done using cubic splines with an exponential truncation but any other function such as in Eq. (15) can be used. It can be seen that around $G = 2.5$ a.u. some points scatter above and below the fitted curve. Indeed, there is no guarantee that the points lie on a smooth curve and the amount of scatter will depend
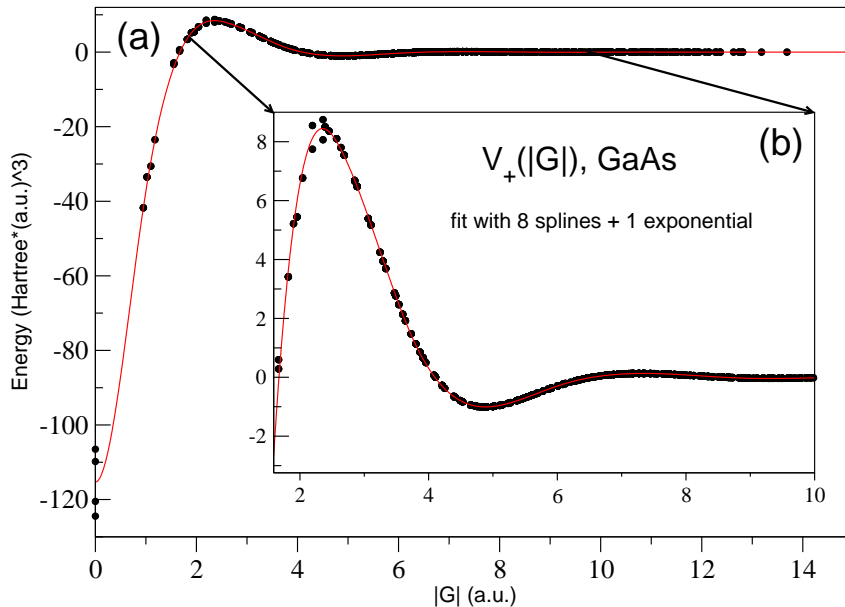
Figure 3: This figure shows one of the steps in the construction of a semiempirical pseudopotential. The points are the DFT results for the screened effective potential for GaAs at discrete **G**-vectors. The line is the fit of our semiempirical pseudopotential through these points.

on the material, the crystal structures and the range of different lattice constants used in the fit. It is also representative of the degree of transferability of the potential. Up to this point, two approximations have been made: (1) The spherical approximation, by going from **G** to $|\mathbf{G}|$ and (2) the average over different crystal structures, by fitting a single curve that passes through several points at a single $|\mathbf{G}|$ value. This procedure turns out to be very accurate for several semiconductors [60, 61] and the overlap of the semi-empirical wave functions, indexed SEPM, and the LDA wave functions, $\langle \psi_i^{\mathrm{LDA}} | \psi_i^{\mathrm{SEPM}} \rangle$, is larger than 99.9% [60, 61].

From the smooth curves fitted through the $v_+(|\mathbf{G}|)$ and $v_-(|\mathbf{G}|)$ points, we obtain the continuous atomic semi-empirical pseudopotentials through Eq. (25). Once this potential is known for each atom type α, we can reconstruct the crystal potential (*Calculate the Crystal Potential* in Fig. 1) by the superposition (as in Eq. (10)),

$$V_{loc}^{\mathrm{SEPM}}(\mathbf{r}) = \sum_{\alpha,j,n} v_\alpha(\mathbf{r} - \mathbf{R}_n - \mathbf{r}_{\alpha,j}) = \frac{1}{\Omega} \sum_{\alpha,j,n} \int_\Omega v_\alpha(|\mathbf{G}|) e^{-i(\mathbf{r} - \mathbf{R}_n - \mathbf{r}_{\alpha,j})\mathbf{G}} \, d^3\mathbf{G} \quad . \quad (27)$$

To reconstruct the full crystal potential we need to include the non-local part of the *ab-initio* ionic pseudopotential $\widehat{V}_{nl}(\mathbf{r})$ (Eq. (20)) . This operator is simply added to the local potential $V_{loc}^{\mathrm{SEPM}}(\mathbf{r})$ (long arrow in Fig. 2) in a fashion very much analogous to the way non-local potentials are treated in DFT [62].

Before the potential can be used to quantitatively predict the properties of nanostructures, two modifications are necessary. One is to reduce the energy cut-off used in the DFT calculation to a value where the quality of the potential/wave functions is not significantly deteriorated but which allows to numerically handle several hundred thousand atoms. Typically energy cut-off values of 5 - 8 Ry have been used [60, 61] in conjunction with an empirical "Gaussian correction" [61]. The second modification is to refit to potential slightly to correct for the known errors of LDA with respect to the bulk band gap and the effective masses. Since these values

are crucial for quantum dots, we need to make sure they agree well with experiment. These last two steps probably give the most part of the empirical "flavor" to the overall methodology. While the first step is of technical nature and for smaller systems (up to ten thousands of atoms at present computational capabilities) the cut-off could be unchanged, the second step might be avoidable by using a quasiparticle approach such as GW, instead of LDA, which gives in some cases very accurate band gaps and effective masses.

2.5 Solving the Schrödinger Equation for the Nanostructure

After having obtained the crystal potential we move on to *solve the Schrödinger equation* in Fig. 1. The Schrödinger equation is given by

$$\widehat{H}\psi_i(\mathbf{r}) = \{-\frac{\nabla^2}{2} + V_{loc}^{\text{SEPM}}(\mathbf{r}) + \widehat{V}_{\text{nl}} + \widehat{V}_{\text{SO}}\}\psi_i(\mathbf{r}) = \varepsilon_i \; \psi_i(\mathbf{r}) \quad . \tag{28}$$

We know that the spectrum of $\widehat{H}$ has an energy gap and we know approximately from the pseudopotential construction at which spectral energy this gap develops. Our aim is to find a dozen of the interior eigenvalues on either side of the gap which determines most of the properties related to excitations. Our aim is therefore not to calculate all the occupied bands, as is customary in DFT approaches, but only a few relevant ones. We therefore have no access to the total energy of the system which requires a sum over all the occupied bands. Since our approach is to represent the total potential by a pseudopotential there is no self-consistent loop to undergo and the Hamiltonian is diagonalized only once. This is another difference to the *ab-initio* ionic pseudopotentials where a self-consistent treatment of the valence electrons is required.

To solve this *interior eigenstate* problem we use [63] a conjugate gradient (CG) type algorithm applied with the Folded Spectrum Method (FSM) [64] or other strategies using state-of-the-art algorithms for the eigenvalue problems at hand, in particular variations of the CG, the locally optimal block preconditioned CG (LOBPCG) [65], and Jacobi-Davidson methods [66].

Depending on the size of the problem we use two different basis sets for ψ_i. For small enough structures, up to a few hundred thousand atoms, we use a simple but large plane wave basis set

$$\psi_i(\mathbf{r}) = \sum_{\mathbf{G}} c_i(\mathbf{G})e^{i\mathbf{G}\cdot\mathbf{r}} \quad , \tag{29}$$

where $\mathbf{G}$ is a reciprocal lattice vector and $c_i(\mathbf{G})$ are the expansion coefficients to be determined variationally. The advantage of the plane wave basis set is that it can be increased systematically and $\widehat{H}\psi$ can be evaluated easily on the fly. The Hamilton matrix is large (dimension can be several millions) and very sparse. Due to its large size the matrix H is never explicitly computed and the solver is matrix free with $\widehat{H}$ acting on each vector ψ. As usual, we calculate the kinetic energy part in Fourier space, where it is diagonal, and the potential energy part in real space where the number of operations required for the matrix-vector product scales as $n \log n$ where n is the dimension of H. We move between Fourier and real space by three dimensional FFTs.

Another basis set is used for larger nanostructures, such as self-assembled quantum dots, and is constructed from a linear combination of strained bulk Bloch states (SLCBB [67]), ϕ_{nk}, from

bands, n, and k-points, k,

$$\psi_i(\mathbf{r}, \epsilon) = \sum_{n,k} c_{n,k}^{(i)} \, \phi_{nk}(\mathbf{r}, \epsilon) \quad, \tag{30}$$

taken at a few strain values ϵ. With this basis set, the Hamilton matrix is rather small, typically n=40,000, but dense and expensive to compute. H is locally stored and solved for a few eigenvectors and eigenvalues using ARPACK [68].

The plane wave code is parallel and can handle hundred thousands of atoms while the SLCBB code is serial but can handle up to millions of atoms due to the underlying assumption in the small basis set used. When it is affordable, the plane wave code is superior because of the possibility to include the non-local potential $\widehat{V}_{nl}$ (while SLCBB can presently only handle local pseudopotentials except for spin-orbit) and because the basis set can be converged systematically by increasing the cut-off energy (while the basis set in SLCBB requires a non-trivial choice from the user for the basis and must be carefully checked for convergence).

2.6 External Constraints and Piezoelectric Field

At this point, a longitudinal external electric fields $\mathbf{E}$ can be added to Eq. (28) [69] through the external potential

$$V_{\text{ext}}(\mathbf{r}) = -\int_{\mathcal{C}} \mathbf{E} \cdot d\mathbf{l} \quad, \tag{31}$$

where $\mathcal{C}$ is an arbitrary path connecting the point with zero potential to the point $\mathbf{r}$.

Constrains such as pressure effects can be naturally investigated [70] since we use an atomistic description and the potentials are constructed to reproduce deformation potentials. The use of a multi-band approach that is not limited to expansion around certain points of the Brillouin zone allows us to investigate transitions that are indirect in k-space [70], such as Γ to L transitions in the conduction band with pressure.

Since our method is non-self-consistent and hence does not allow for long ranged charge redistributions, it neglects effects such as piezoelectricity where charge is moved due to strain. In this case, the piezoelectric potential must be calculated independently [71, 72] and added as an external potential, just like in the case of "truly" external fields. This is *a priori* difficult for large structures but through a combination of strain calculations that can be done with empirical force fields and DFT calculations for the piezoelectric response we can obtain the necessary potential [71]. It turns out that second order effects in strain need to be taken into account [71] to obtain reliable results.

2.7 Solution of the many-body problem

2.7.1 Correlations in the Ground State

The word *correlation* in the context of quantum dots can lead to some confusions that we intend to prevent by this short section. Correlations are usually defined as the difference between the Hartree-Fock ground state and the exact many-body solution. In this context, correlations are purely a ground state property. The conventional quantum chemical methods start from the Hartree-Fock (HF) single-determinant ground state and use configuration interaction (CI),

Møller Plesset, coupled cluster (CC), among other methods, to add correlations to the ground state. We, however, do not attempt to solve the many-body problem for the ground state, since it consists of thousands of electrons. Our approach is purely empirical at this stage: we assume that the solutions of our Schrödinger equation (Eq. (28)) with the effective empirical pseudopotential are already fully correlated quasiparticle eigenfunctions and quasiparticle eigenvalues. The fact, that our pseudopotential is local or semi-local while the true quasiparticle equation is fully non-local points to the underlying approximation.

2.7.2 Correlations in the excitation: Configuration Interaction

Once the quasiparticle eigenfunctions have been calculated we follow the configuration interaction (CI) method (see Fig. 1) to obtain the excitations (such as an exciton) of the system. At this point, the correlations of the ground state are assumed to be decoupled from the correlations of the excitation. This is justified by the Brillouin theorem which states that there is no coupling between the Hartree-Fock (HF) ground state and the single-exciton ("singles") excitation $|\Phi_{h_i,e_j}\rangle$. Note that we are not starting from the HF ground state, as in the Brillouin theorem, but from the solution of the quasiparticle equation. It can still be shown [27] that $|\Phi_{h_i,e_j}\rangle$ and $|\Phi_0\rangle$ are decoupled. There is, however, coupling between the higher excitations such as double-exciton excitation ("doubles") and the ground state. These are neglected in our approach, which can be justified by the fact that doubles are energetically remote from the ground state.

The correlations in the excitation are treated at the level of "singles" only, i.e., only single-exciton excitation where one hole in the valence band and one electron in the conduction band are created, are allowed to interact. Formally, the correlated exciton wave function can be constructed from a set of Slater determinants [73, 74]:

$$|\Phi_{h_i,e_j}\rangle = b_{h_i}^\dagger c_{e_j}^\dagger |\Phi_0\rangle \tag{32}$$

where $b_{h_i}^\dagger$ is the creation operator for holes and $c_{e_j}^\dagger$ the creation operator for electrons. The Slater determinants $|\Phi_{h_i,e_j}\rangle$ can be calculated from anti-symmetrized products of single-particle wave functions ψ_i from equation (28).

The exciton wave functions $|\Psi\rangle$ are expanded in terms of this determinental basis set:

$$|\Psi\rangle = \sum_{h_i,e_j} A(h_i, e_j)|\Phi_{h_i,e_j}\rangle \quad , \tag{33}$$

where A are the expansion coefficients and we use i to index hole states and j to index electron states. The Slater rules [73] allow us to express the matrix elements between Slater determinants in terms of one– and two–center integrals:

$$\langle \Phi_{h_i,e_j}|H|\Phi_{h_{i'},e_{j'}}\rangle = (\varepsilon_{e_j} - \varepsilon_{h_i})\delta_{h_i h_{i'}}\delta_{e_j e_{j'}} + \langle e_j h_{i'}|v|h_i e_{j'}\rangle - \langle e_j h_{i'}|v|e_{j'} h_i\rangle \quad , \tag{34}$$

with the two center integrals

$$\langle e_j h_i|v|h_{i'} e_{j'}\rangle = \iint \psi_j^\star(\mathbf{r}_e)\psi_i^\star(\mathbf{r}_h)v(\mathbf{r}_e,\mathbf{r}_h)\psi_{i'}(\mathbf{r}_e)\psi_{j'}(\mathbf{r}_h)\,\mathrm{d}\mathbf{r}_e\,\mathrm{d}\mathbf{r}_h \quad , \tag{35}$$

using $v(\mathbf{r}_e, \mathbf{r}_h)$ for the screened Coulomb interaction described in the next section. The last term in Eq. (34) describes the direct Coulomb integrals and the one before last the exchange integrals. The formalism described from Eq. (32) to Eq. (35) can be generalized to the case of an arbitrary number of electrons and holes and is not limited to the case of excitons. For the case of multiexcitons or charged excitons, the subspace of Slater determinants included in Eq. (32) has been restricted to excitations that conserve the number of electrons and the number of holes. For instance, a biexciton state has been constructed from Slater determinants with two electrons and two holes (double excitation), neglecting the coupling to Slater determinants with one electron and one hole (singles). This coupling is non zero, but rather small since the energy difference between the single and the double excitations is approximately given by the band gap. This generalization from the exciton case to an arbitrary number of electrons and holes, represents one of the advantages of this approach. In our numerical treatment, equations such as (34) are not directly implemented but rather the action of creation and annihilation operators in a general second quantization form.

2.7.3 Screening

In quantum chemistry, configuration interaction is often treated at the level of triples, quadruples, all the way to *full* CI which exactly solves the electronic Schrödinger equation within the space spanned by the one-particle basis set. In these calculations, the integrals (35) are the bare unscreened ($v(\mathbf{r}_e, \mathbf{r}_h) = 1/(|\mathbf{r}_e - \mathbf{r}_h|)$) Coulomb integrals. For excitations in a nanostructure, such an approach is computationally not feasible using an atomistic description and we have to limit ourselves in the one-particle basis set to only few states close to the band gap and to single excitations only. To neglect the coupling of singles to higher excitations is a poor approximation. However, it can be shown that the effect of higher order excitations can be folded back onto the considered subspace of single excitations [27,75]. The effect of this procedure is to renormalize (screen) the Coulomb interactions, as we already indicated in Eq. (35) by $v(\mathbf{r}_e, \mathbf{r}_h)$. There was, and partly still is, some debate about the screening of the electron-hole exchange terms that was recently addressed via field theory arguments [75]. It was argued [75] that in the limiting case where transitions are considered over a wide energy range the electron-hole exchange term should be unscreened while in the limiting case where only the few lowest energy transitions are considered (usually our case) the interaction should be screened by the full dielectric function.

Besides this rather fundamental issue of whether to screen or not screen the interactions, the choice of the dielectric function is another important and developing theme. The screened Coulomb potential from Eq. (35) can be generally written as

$$v(\mathbf{r}_e, \mathbf{r}_h) = e^2 \int \epsilon^{-1}(\mathbf{r}_e, \mathbf{r}) |\mathbf{r} - \mathbf{r}_h|^{-1} \, d\mathbf{r} \quad , \tag{36}$$

with the inverse dielectric function $\epsilon^{-1}(\mathbf{r}_e, \mathbf{r})$. For large nanostructures, the screening function used has been directly taken from the literature for bulk systems. We used [76] the phenomenological isotropic and uniform ($\epsilon(\mathbf{r}_e, \mathbf{r}_h) \simeq \epsilon(|\mathbf{r}_e - \mathbf{r}_h|)$) model proposed by Resta [77] for the electronic screening and by Haken [78] (for the case of the exciton) for the ionic part: $\epsilon^{-1} = \epsilon_{el}^{-1} + \epsilon_{ion}^{-1}$ with

$$\epsilon_{el}^{-1}(k) = \frac{k^2 + q^2 \sin(k\rho_\infty)/(\epsilon_\infty k\rho_\infty)}{k^2 + q^2}, \quad \epsilon_{ion}^{-1}(k) = \left(\frac{1}{\epsilon_0} - \frac{1}{\epsilon_\infty} \right) \left(\frac{1/2}{1 + \rho_h^2 k^2} + \frac{1/2}{1 + \rho_e^2 k^2} \right), \tag{37}$$

with q the Thomas-Fermi wave vector, ρ_∞ is the solution of $\sinh(q\rho_\infty)/(q\rho_\infty) = \epsilon_\infty$ and $\rho_{h,e} = (\hbar/2m^*_{h,e}\omega_{\text{LO}})^{1/2}$, with $m^*_{h,e}$ the hole and electron effective masses and ω_{LO} the bulk LO-phonon frequency.

For small nanostructures the approximation of bulk screening is not appropriate since the effect of the interface plays an increasing role. A screening function depending on the radius of a spherical nanostructure was used for colloidal quantum dots [74]. The high frequency bulk dielectric constant ϵ_∞ from Eq. (37) was replaced [74] by a constant $\epsilon_\infty^{\text{dot}}$ obtained from a modified Penn model where the size dependence enters the equation through the value of the optical band gap of the dot [74]. The low frequency dielectric constant of the dot ϵ_0^{dot} was obtained simply by keeping $\epsilon_0^{\text{dot}} - \epsilon_\infty^{\text{dot}} = \epsilon_0 - \epsilon_\infty$. In this approach, the dielectric function remains dependent on the distance $|\mathbf{r} - \mathbf{r}'|$ but is independent of the position $\mathbf{r}$, i.e., screening is modified (typically reduced) throughout the nanostructure.

More recently, truly position dependent dielectric functions have been derived from tight binding calculations [79] and from density functional theory [80] for nanostructures. The screening function is obtained from the induced response of the system to an external perturbation, such as a delta-function or Coulomb-like perturbation of the potential. These calculations suggest that the screening function remains "bulk-like" inside the core of the structure and changes only in the close proximity of the interface.

2.7.4 Dielectric Mismatch and Polarization Charges

In the discussion of the screening function and the single-particle Schrödinger equation we did not mention the fact that the nanostructures are usually surrounded by a material with different dielectric properties. In this case, polarization charges appear on the surface of the nanostructure which have effects on the self-energy [81] and on the two particle binding energy [82]. Indeed, the dielectric mismatch leads to a surface polarization potential which corresponds to the classic electrostatic potential caused by a point charge inside an object, similarly to the image potential created by a point charge close to a dielectric medium. Quantum mechanically, the effect can be treated as an additional on-site potential $P(\mathbf{r})$ in the Schrödinger equation Eq. (28) [81]:

$$\widehat{\text{H}}\psi_i(\mathbf{r}) = \{-\frac{\nabla^2}{2} + V^{\text{SEPM}}_{loc}(\mathbf{r}) + \widehat{\text{V}}_{\text{nl}} + \widehat{\text{V}}_{\text{SO}} + P(\mathbf{r})\}\psi_i(\mathbf{r}) = \varepsilon_i\,\psi_i(\mathbf{r}) \quad . \tag{38}$$

This additional potential leads to a modification of the quasiparticle eigenvalues that we label as Σ_c^{surf} for the conduction band and Σ_v^{surf} for the valence band. The terms $\Sigma_{c,v}^{\text{surf}}$ vanish for $\epsilon_{\text{in}} = \epsilon_{\text{out}}$ and are positive for the conduction band and negative for the valence band in case $\epsilon_{\text{in}} > \epsilon_{\text{out}}$, i.e. both contribute to an increase of the quasiparticle gap.

The dielectric mismatch and the ensuing surface polarization has an effect on the screened Coulomb interaction between the two quasi-particles. In addition to the direct Coulomb interaction we discussed previously, there is an additional interaction between one of the quasi-particles and the image surface charge of the other. This effect results in a modification of the direct Coulomb interaction J^{dir} by a surface polarization term J^{pol}. It can be shown [27, 83] that for spherical nanocrystals the contributions from the surface self-energy terms to the exciton $\Sigma_e^{\text{surf}} + \Sigma_h^{\text{surf}}$ mostly cancel the surface polarization contribution to the Coulomb term J^{pol}. It is therefore a common approximation [23, 74], when dealing with excitons in nearly

spherical colloidal quantum dots, to neglect the effects of polarization charges altogether, i.e., in the quasiparticle picture by using a simplified Schrödinger equation such as Eq. (28) and in the exciton problem, by neglecting the surface polarization term. On the other hand, for non-spherical nanostructures but with small dielectric mismatch, such as in self-assembled embedded quantum dots, the polarization terms $\Sigma_{e,h}^{\mathrm{surf}}$, $\Sigma_{e,h}^{\mathrm{surf}}$ and J^{pol} are often assumed to be small [76]. For non-spherical colloidal nanostructures such as tetrapods [84] or dumbbells [85], where dielectric mismatch is usually large, the polarization terms must be explicitly taken into account [27, 84]. Also in the calculation of charging energies or charged excitons, where the cancellation of self-energy and surface polarization is not given, effects of dielectric mismatch must be included [83].

2.7.5 Discussion

Before we move on to the next step where the many-body wave functions will be used to calculate observables, we will summarize in a qualitative and rather schematic manner the computational scheme used so far. In Fig. 4 we give an overview of the different energetic contributions to the band gap of a semiconductor or insulator. The left side of the Figure [a) LDA] corresponds to the band gap obtained with a single-particle description of the ground state such as density functional theory in the local density approximation (LDA). The band gap $\varepsilon_c^0 - \varepsilon_v^0$ is typically underestimated. The error in the band gap is mainly due to a missing or incorrect description of the self-energy $\Sigma_{\mathrm{bulk}}^{e,h}$. In Hedin's GW approximation [86], at the quasiparticle level, this contribution is properly accounted for and the band-gap opens up [b) GW]. The next column [c) LDA] describes the situation in a nanostructure where in the single-particle case, the band gap opens up by $E_{\mathrm{conf}}^{e,h}$ because of confinement. $E_{\mathrm{conf}}^{e,h}$ depends on the size of the nanostructure, the band structure (effective mass) of the material, the strain and deformation potentials. In the next column [d) GW], at the GW level, the contributions of $\Sigma_{\mathrm{bulk}}^{e,h}$ add up but also the contributions due to surface polarization effects $\Sigma_{\mathrm{surf}}^{e,h}$ described in the previous section 2.7.4. Our empirical pseudopotential method enters the picture at the level given in "e) EPM" where the self-energy contributions to the bulk $\Sigma_{\mathrm{bulk}}^{e,h}$ are taken into account but not the ones of surface polarization $\Sigma_{\mathrm{surf}}^{e,h}$. In the right column [f) Exciton], the optical band gap is given, where the Coulomb interaction, J_{pol}^{eh}, and J_{direct}^{eh}, contribute to reduce the band gap. J_{pol}^{eh}, and J_{direct}^{eh} have been artificially split into two parts $J_{\mathrm{pol}}^{eh,1,2}$, and $J_{\mathrm{direct}}^{eh,1,2}$ to be able to visually include the two-particle excitonic description of the right column within the single-particle and quasiparticle description of columns a)-e). As discussed in section 2.7.4 the terms $\Sigma_e^{\mathrm{surf}} + \Sigma_h^{\mathrm{surf}}$ tend to cancel $J_{\mathrm{pol}}^{eh} = J_{\mathrm{pol}}^{eh,1} + J_{\mathrm{pol}}^{eh,2}$ for spherical nanostructures. In the case of no dielectric mismatch between the nanostructure and the environment, the terms Σ_e^{surf}, Σ_h^{surf} and J_{pol}^{eh} vanish.

2.8 Post-Processor Tools

After we have calculated the many-body wave function we have access to observables through the use of post-processor tools as shown in the last step of the flowchart in Fig. 1 .
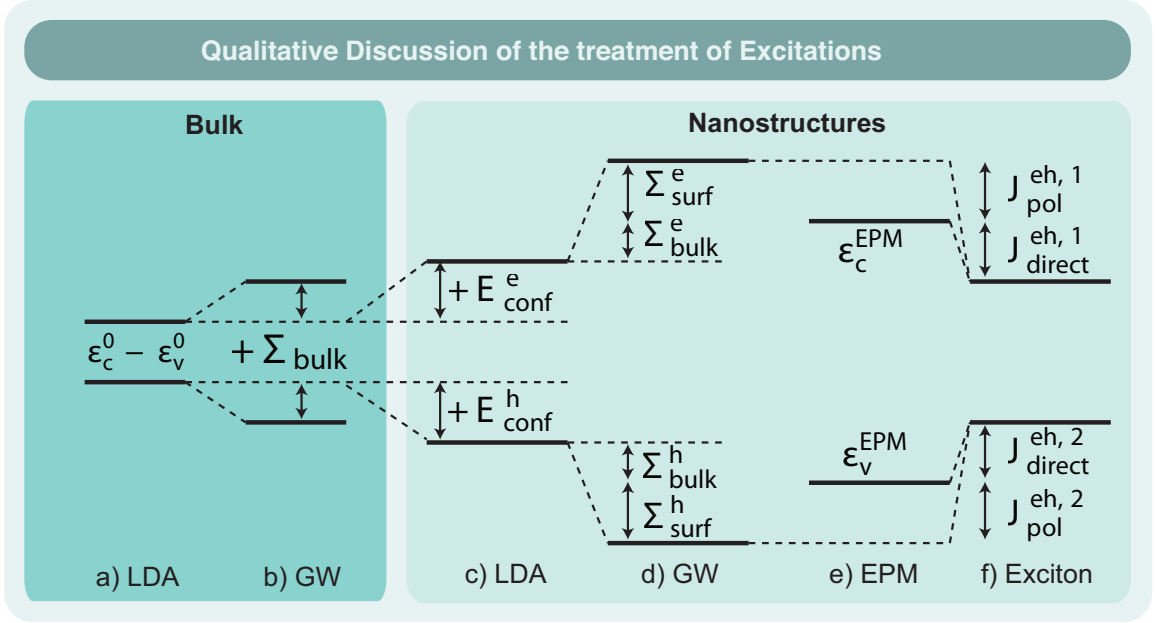
Figure 4: Qualitative description of the position of the conduction band minimum (or LUMO) and valence band maximum (or HOMO) in different theoretical approaches. See section 2.7.5.

2.8.1 Optics

The optical properties of semiconductor nanostructures are among the most relevant observables. The optical transition of an excitonic complex χ to the excitonic complex $(\chi - 1)$, where one electron-hole pair has been annihilated, is characterized by both the transition energy between the initial state i and the final state f, $\omega_{if}(\chi)$, and the optical transition dipole matrix element

$$M_{if}^{(\hat{\mathbf{e}})}(\chi) = \langle \Psi^{(f)}(\chi - 1)|\hat{\mathbf{e}} \cdot \mathbf{p}|\Psi^{(i)}(\chi)\rangle \quad , \tag{39}$$

with the momentum operator $\mathbf{p}$ and the polarization vector of the electromagnetic field $\hat{\mathbf{e}}$ [87,88]. The oscillator strength for the exciton complex χ and for polarization $\hat{\mathbf{e}}$ is given by

$$\alpha^{(\hat{\mathbf{e}})}(\omega, T; \chi) \propto \sum_{i,f} \left|M_{if}^{(\hat{\mathbf{e}})}(\chi)\right|^2 P_i(T; \chi)\,\delta(\omega - \omega_{if}(\chi)) \quad , \tag{40}$$

where

$$P_i(T; \chi) = \mathcal{N} \exp\{-[E^{(i)}(\chi) - E^{(0)}(\chi)]/k_B\,T\} \tag{41}$$

is the occupation probability of the initial state $|\Psi^{(i)}(\chi)\rangle$ at temperature T and $\mathcal{N}$ is a normalization constant. The delta function can be replaced by a Gaussian to account for size distribution (inhomogeneous broadening) or by a Lorentzian to account for intrinsic sources of broadening (homogeneous broadening). We can define a radiative lifetime, $\tau_{if}(\chi)$, that is specific to the transition between states i and j as:

$$\frac{1}{\tau_{if}(\chi)} \propto n\,\omega_{if}(\chi) \sum_{\hat{\mathbf{e}}=\hat{x},\hat{y},\hat{z}} \left|\mathbf{M}_{if}^{(\hat{\mathbf{e}})}(\chi)\right|^2 \quad , \tag{42}$$

where, e and m_0 are the charge and mass of the electron, respectively, c is the velocity of light in vacuum and n is the refractive index of the dot material. The underlying assumption in Eq. (42) that guarantees a simple linear dependence of $1/\tau_{if}(\chi)$ on refractive index is a similar dielectric

constant inside and outside the nanostructure, as is the case of many embedded self-assembled quantum dots. In a more general case, more complicated dependences have been proposed [89].

Note that the "specific" radiative lifetime defined in Eq. (42) does not depend on temperature nor on the occupation probabilities of the states while the actual (measured) radiative lifetime $\tau(\chi)$ depends non-trivially on occupation probabilities. To obtain the actual lifetime, the time dependent Schrödinger equation has to be solved. This can be done by reducing the problem to a few level system and by solving a set of master equations [88, 90].

2.8.2 Quantum Entanglement

With our CI results we have access to quantum mechanical quantities related to correlations, such as quantum entanglement. Entanglement is one of the most important quantities for successful quantum gate operations and it is interesting to quantify the amount of entanglement present, or achievable, given a certain system. The degree of entanglement of *distinguishable* particles can be calculated from the von Neumann-entropy formulation [91, 92]. For example for a two component system (A, B), it is defined as, [91–93]

$$\mathcal{S} = -\operatorname{Tr} \rho_A \log_2 \rho_A = -\operatorname{Tr} \rho_B \log_2 \rho_B , \qquad (43)$$

where, ρ_A and ρ_B are the reduced single-particle density matrices of the subsystems A and B. However, there are some subtleties for defining the degree of entanglement for *indistinguishable* particles, since it is impossible to separate the subsystems A and B. Recently, we have derived a generalization of the von Neumann definition [94, 95] for *identical* particles through a Slater decomposition [96, 97] where the maximum entanglement of a two-electron system is $\mathcal{S} = \log_2 N$, where N is the number of available single-particle states. Our definition reduces to Eq. (43) when the two-electrons are far from each other [94, 95].

2.8.3 Tunneling Experiments

From the many-body wave functions we can obtain informations relevant to tunneling and optical experiments such as scanning tunneling microscopy (STM), magnetotunneling spectroscopy (MTS) or near-field scanning optical microscopy (NSOM or SNOM). For the case of STM and MTS, we calculate [20] the transition probability of an electron or hole from an emitter in state κ to a quantum dot containing N particles from the expression $\frac{2\pi}{\hbar}|\mathcal{M}_{\kappa,N}|^2 n(\varepsilon_F)$ [98] where $n(\varepsilon_F)$ is the enegy of the final quantum dot states. The transition matrix elements $\mathcal{M}_{\kappa,N}$ for the transfer of one particle from the emitter in state κ to the quantum dot state $|N\rangle$, filled by N electrons, can be factorized [99] as $\mathcal{M}_{\kappa,N} \propto T_\kappa M_{\kappa,N}$ where T does not depend on N, nor on the coordinates in-plane, x,y (if z is the tunneling direction). The relevant matrix element is therefore $M_{\kappa,N}$ and is given by:

$$M_{\kappa,N} = \int \phi_\kappa^*(\mathbf{x})\Psi_{\mathrm{QD}}(\mathbf{x})d\mathbf{x} \quad . \qquad (44)$$

Here, $\phi_\kappa^*(\mathbf{r})$ is the probing or emitter wave function and $\Psi_{\mathrm{QD}}(\mathbf{x})$ is the quasi-particle excitation between the $N-1$ particle states $|N-1\rangle$ and the N particle states $|N\rangle$, i.e.,

$$\Psi_{\mathrm{QD}}(\mathbf{x}) = \sum_i \langle N-1|\hat{c}_i|N\rangle \psi_i(\mathbf{x}) \quad . \qquad (45)$$

58

$\psi_i(\mathbf{x})$ is the atomistic ith single-particle wave function and $\hat{c}_i$ is an electron (hole) annihilation operator. The correlated many-body states are obtained, as described in section 2.7, by configuration interaction:

$$|N\rangle \;=\; \sum_\beta C_\beta^{(N)} \Phi_\beta(\mathbf{x}_1, \cdots, \mathbf{x}_{N-1}, \mathbf{x}_N) \quad, \tag{46}$$

and

$$M_{\kappa,N} = \sum_i \langle N-1|\hat{c}_i|N\rangle \langle\phi_\kappa|\psi_i\rangle = \sum_i \sum_{\alpha,\beta} C_\alpha^{*(N-1)} C_\beta^{(N)} \langle\Phi_\alpha^{(N-1)}|\hat{c}_i|\Phi_\beta^{(N)}\rangle \, \langle\phi_\kappa|\psi_i\rangle \tag{47}$$

with

$$\langle\Phi_\alpha^{(N-1)}|\hat{c}_i|\Phi_\beta^{(N)}\rangle = \begin{cases} 1 & \text{if } |\Phi_\alpha^{(N-1)}\rangle = \hat{c}_i|\Phi_\beta^{(N)}\rangle, \\ -1 & \text{if } |\Phi_\alpha^{(N-1)}\rangle = -\hat{c}_i|\Phi_\beta^{(N)}\rangle, \\ 0 & \text{otherwise.} \end{cases}$$

where i indexes the single particle states obtained from the solution of Eq. (28).

There are different techniques to probe the quasi-particle excitations. For example, in scanning tunneling microscopy experiments, the probing wave function $\phi_\kappa(\mathbf{x})$ can be represented by a δ-function at a given real space point, $\phi(\mathbf{x}) \sim \delta(\mathbf{x})$, in which case the transition rate is given by $\sim |\psi_{\mathrm{QD}}(\mathbf{x})|^2$ and maps out the square of the quasi-particle excitations in real space.

An alternative approach is taken in MTS where the quasiparticle excitations are mapped out in reciprocal space. Using an atomistic description, the probing wave functions can be written as a Bloch function $\bar{u}_\mathbf{k}$ modulated by a plane wave:

$$\phi_\mathbf{k}(\mathbf{x}) = \bar{u}_\mathbf{k}(\mathbf{x})e^{i\,\mathbf{k}\cdot\mathbf{x}} \quad. \tag{48}$$

The atomistic wave functions for the quantum dot states can be written as:

$$\psi(\mathbf{x}) = \sum_n^{N_B} \sum_\mathbf{k}^{N_k} c_{n,\mathbf{k}}\, u_{n,\mathbf{k}}(\mathbf{x})\, e^{i\mathbf{k}\cdot\mathbf{x}} \tag{49}$$

where $u_{n,\mathbf{k}}(\mathbf{x})$ are Bloch wave functions with band index n and k-points $\mathbf{k}$ [20, 100] so that the product $\langle\phi_\kappa|\psi_i\rangle$ in Eq. (47) is given by:

$$\langle\phi_\mathbf{k}|\psi_i\rangle = \sum_n^{N_B} \langle\bar{u}_\mathbf{k}|u_{n,\mathbf{k}}\rangle c_{n,\mathbf{k}} \quad. \tag{50}$$

The overlap $\langle\bar{u}_\mathbf{k}|u_{n,\mathbf{k}}\rangle$ is largest at the interface and since we do not know the exact form of the Bloch part of the probing wave function, we have to resort to certain approximations. We assumed [20, 100] a constant $\langle\bar{u}_\mathbf{k}|u_{n,\mathbf{k}}\rangle$ in which case $M_{\kappa,N}$ in Eq. (47) is a function of $\mathbf{k}$ and N that can be directly calculated.

2.9 Charging Energies

The charging energy $\mu(N)$ is the energy necessary to add one more carrier to the dot already charged by $N-1$ carriers:

$$\mu(N) = E(N) - E(N-1) \quad, \tag{51}$$

where $E(N)$ are the correlated many-body total energies of the ground states of the N-particle dot. The addition energy $\Delta(N-1, N)$ indicates how much more energy is needed to add the Nth carrier compared to the energy needed to add the $(N-1)$th carrier:

$$
\begin{aligned}
\Delta(N-1, N) &= \mu(N) - \mu(N-1) \\
&= E(N) - 2E(N-1) + E(N-2) \quad .
\end{aligned}
\tag{52}
$$

The charging and addition energies are therefore directly obtained from the many-body energy calculated using the configuration interaction approach described in section 2.7 and can directly be compared to experiment.

3 Applications

Extensive work has been done recently using the empirical pseudopotential methodology on the material system InAs and GaAs [20, 26, 56, 69–72, 76, 88, 93–95, 100–104] and CdSe [74, 104–110]. Beyond these materials —in the focus of attention because of the wide availability of experimental results— potentials for InAs/InSb [111], PbSe [112, 113], InP/GaP [74, 114], nitrides [58, 115], among others, have been developed for embedded structures and for colloidal nanocrystals with adequate surface passivations. We will not attempt to review these many results but will rather select a few examples that should emphasize the generality of the method and its accuracy, able to predict new and unexpected physics.

3.1 Optics and Fine Structure

The term *fine structure* has been used in the realm of nanostructure physics to describe the small splittings due to the electron-hole exchange interaction. In the simplest case when the electron and hole states are derived from a single Kramers doublet, four possible electron-hole state combinations emerge due to the particle's pseudospins (indicated with arrows): $|e\uparrow\, h\uparrow\rangle$, $|e\uparrow\, h\downarrow\rangle$, $|e\downarrow\, h\uparrow\rangle$, $|e\downarrow\, h\downarrow\rangle$. The electron-hole exchange integrals are special cases of the integrals given in Eq. (35) and can be rewritten as:

$$
K_{ij',ji'} = \iint \psi_i^\star(\mathbf{r}_e)\psi_{j'}^\star(\mathbf{r}_h)v(\mathbf{r}_e,\mathbf{r}_h)\psi_j(\mathbf{r}_e)\psi_{i'}(\mathbf{r}_h)\,\mathrm{d}\mathbf{r}_e\,\mathrm{d}\mathbf{r}_h \quad ,
\tag{53}
$$

where we have kept the notation that i, i' indexes hole states and j, j' indexes electron states. The "exchange" of particle can be seen from Eq. (53) through the fact that at position $\mathbf{r}_e$ a hole wave function is on the left of v but an electron wave function on the right. These integrals lead to the splitting of the four electron-hole pairs and to the appearance of the fine structure. The integrals given in Eq. (53) require knowledge about the details of the Bloch part of the wave function which is naturally given by an atomistic description [76] but not readily available in envelope function theories. The integrals from Eq. (53) are sensitive to the effects of spin-orbit interaction, the atomistic symmetry, band mixing and to the full range of screening (long- and short-range) [76].

The atomistic calculation of fine structure splittings [72, 76, 88, 116, 117] and the comparison of the results with experiments [116] is an excellent benchmark for the theory and leads to

an understanding of the experimental results otherwise difficult or impossible to obtain. To illustrate the physical insight that can be obtained, we choose the example of the fine structure of the X^{2-} charged exciton shown in Fig. 5. On the left side (Fig. 5 a)) we show the initial configuration that consists of three electrons and one hole and the final configuration, after the recombination of one electro-hole pair, which consists of two electrons. Four many-body levels can be constructed from the limited set of one hole state h_0 and two electron states e_0 and e_1. Since the electrons in state e_0 must be paired, only the configurations $|(e_0\!\uparrow\ e_0\!\downarrow)e_1\!\uparrow\ h_0\!\uparrow\rangle$, $|(e_0\!\uparrow\ e_0\!\downarrow)e_1\!\uparrow\ h_0\!\downarrow\rangle$, $|(e_0\!\uparrow\ e_0\!\downarrow)e_1\!\downarrow\ h_0\!\uparrow\rangle$, $|(e_0\!\uparrow\ e_0\!\downarrow)e_1\!\downarrow\ h_0\!\downarrow\rangle$, are possible, much like in the case of a single electron-hole pair mentioned previously. Note that this is only a simplifying model that helps us to understand the results which do take many more configurations into account. Indeed, the number of configurations included in the CI treatment (section 2.7.2) is given by

$$N_{\text{conf}} = \frac{b_c!}{n_e!(b_c - n_e)!} \frac{b_v!}{n_h!(b_v - n_h)!} \quad , \tag{54}$$

where n_h and n_e are the number of holes and electrons, respectively, distributed among b_v and b_c valence and conduction band states, counting spin. For the initial state of Fig. 5 a) with a configuration space of 10 electron and 10 hole states (i.e., counting spin, $b_c = b_v = 20$) we have 22800 mixing configurations. However, an analysis such as the one in Fig. 5 a) describes most of the physics properly in this case. Some striking deviations of the simple model have been addressed in Ref. [117]. The electron-hole exchange interaction splits the four levels of X^{2-} into a doublet and two singlets in the initial state and the electron-electron exchange interaction splits the final state into a singlet and a triplet state. The magnitude of the electron-electron and the electron-hole interaction is significantly different, the latter being more than an order of magnitude smaller than the former, with splittings in the order of tens of μeV. From the initial to the final many-body states we can anticipate six transitions as marked in Fig. 5 a), 1-3 are split from 4-6 by electron-electron exchange, while 1-3 and 4-6 are themselves split by the small electron-hole exchange interaction. The optical transitions that connect initial and final states can be calculated using the formalism described in section 2.8.1. The theoretical results for the oscillator strength for a lens shaped InAs self-assembled quantum dot embedded in GaAs are given in Fig. 5 b) and the corresponding experimental results in Fig. 5 c). The transition "1" from Fig. 5 a) has vanishing oscillator strength and therefore dark. The transitions are also polarized along certain crystallographic directions giving us a useful tool to clearly identify transitions and their origin [116, 117].

3.2   Entanglement

The field of nanostructure science is increasingly driven by efforts aimed at using the electrons in confined geometries to realize different schemes of quantum information science, where the physical information is held in the *state* of the quantum system. This represents an area of science where quantitative theories able to predict many-body properties of realistic systems are important. Some prominent examples are the proposal to use two vertically [118, 119] or laterally [120] coupled quantum dots containing two electrons [17], or an exciton [121] to perform some basic gate operations. The carrier of quantum informations, the qubits, can be realized by either the spin of the electron [17] or by the location of an electron or hole [121]. Our methodology
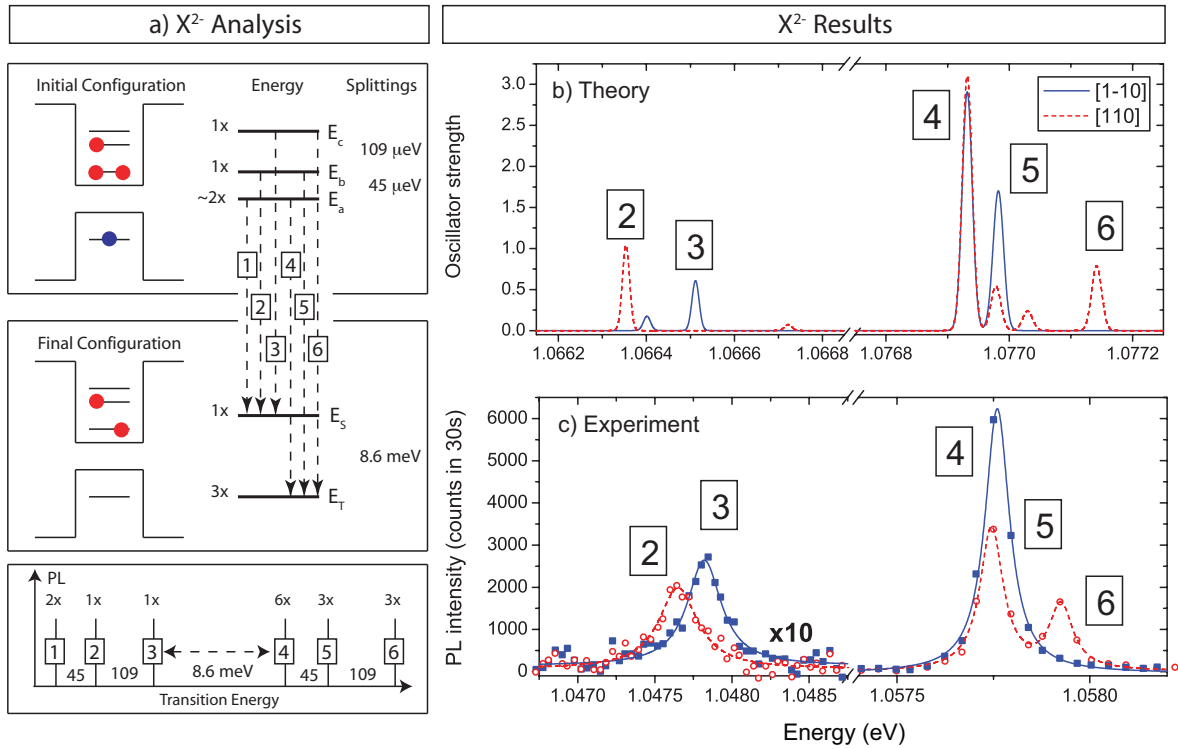
Figure 5: Fine structure of the X^{2-} charged exciton in a self-assembled InAs quantum dot. a) Analysis of the results in a simplified picture where only few many-body states for the initial and final states are considered. Note that the splitting of the initial states is given in μeV while the splitting of the final states in meV. b) Theoretical results for the oscillator strength in arbitrary units. c) Experimental results. Figure adapted from Ref. [116].

gives us access to some of the relevant quantities such as the degree of entanglement between the two electrons [94, 95] or between the electron and the hole [69, 93, 101], or the singlet-triplet splitting [95]. These quantities are sensitive to the geometry of the system, spin-orbit interaction, the amount of strain, and only a methodology that takes these effects into account can give a quantitative prediction.

In Figure 6 we present the results obtained for an InGaAs quantum dot molecule with dimensions and composition taken from experiment [121] as 12 nm in diameter and 2 nm height with a graded In-composition profile [69]. The two dots are vertically stacked, around 8 nm apart. A fully entangled electron-hole pair can be represented by the the maximally entangled Bell state $|e_T h_T\rangle + |e_B h_B\rangle$, where e and h stand for the electron and the hole (the two qubits) and T and B for their localizations in top or bottom dot (the state of the qubits). The entropy of entanglement is calculated according to Eq. (43) where A is the reduced density matrix for qubit A (the electron) and B is the reduced density matrix for qubit B (the hole). The density matrices are calculated from the correlated CI exciton density which requires a projection of the exciton wave functions on the dot localized basis set [69]. From the right side of Fig. 6 we can see that the degree of entanglement as a function of electric field is peaked at a certain electric field achievable experimentally [122–126] (5.4 kV/cm in our specific case) and can reach 80%. The left side of Fig. 6 shows that at this specific electric field the peaks in oscillator strength originating from the exciton states $|1\rangle$ and $|2\rangle$ anticross and $|1\rangle$ becomes dark. This optical signature may be used by experimentalists in the future to identify the electric field needed to achieve maximum entanglement in specific dot molecules. The theoretical results can be further

analyzed to understand, in terms of electron and hole localization on either one of the two dots, the way the particles conspire to create entangled states and what are the limiting and driving factors [69, 101] such as the effect of geometry, composition, dot-separation and the ensuing strain on tunneling and Coulomb interactions. From this understanding we could construct a simplified model hamiltonian with few and well defined parameters [93].
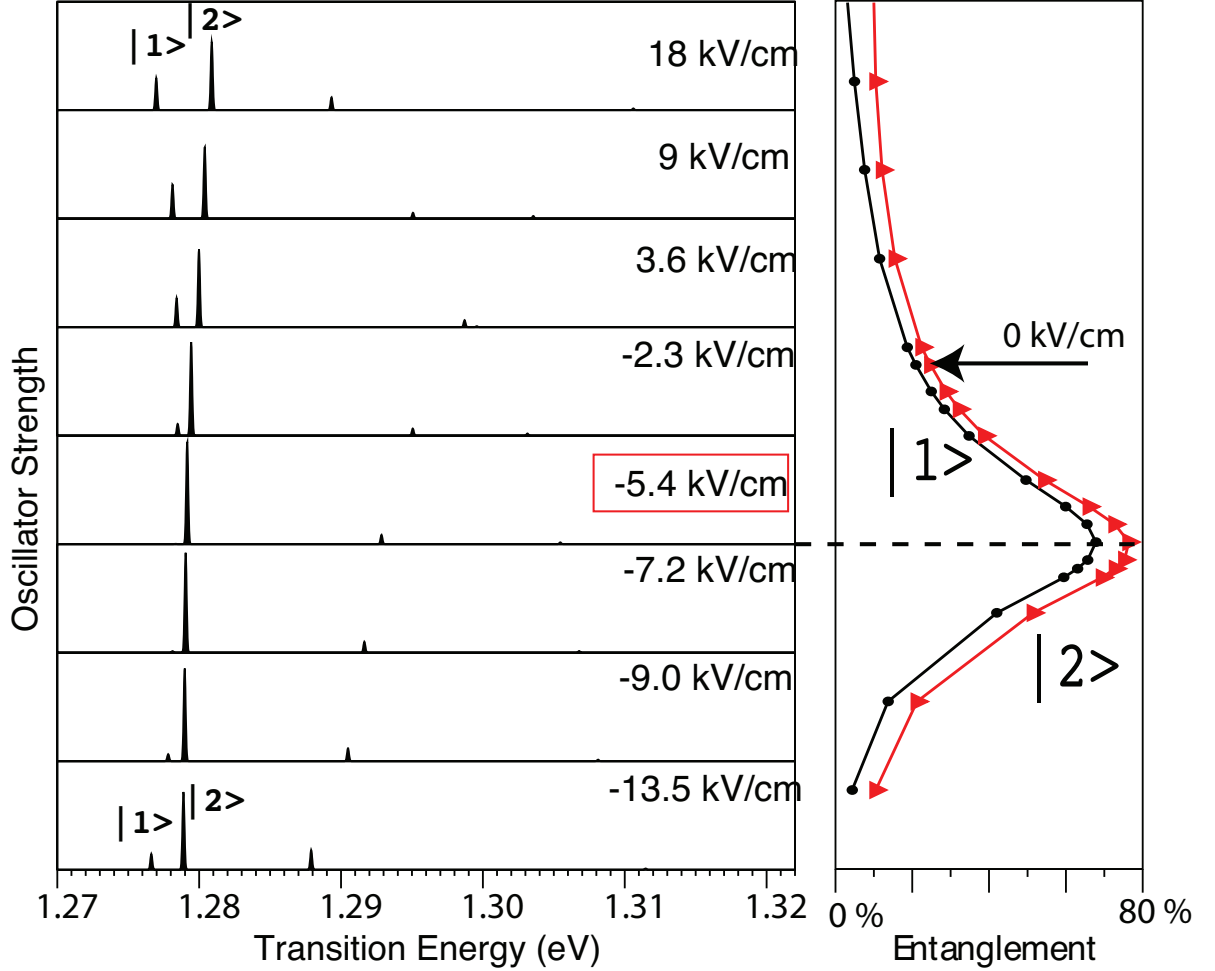
Figure 6: Electric field dependence of the oscillator strength (left) and the entropy of entanglement (right) of the two exciton states $|1\rangle$ and $|2\rangle$ in an InGaAs self assembled quantum dot embedded in GaAs. At the critical field of 5.4 kV/cm, applied in growth direction, the entanglement is maximized and the two peaks in the oscillator strength originating from $|1\rangle$ and $|2\rangle$ anticross and $|1\rangle$ becomes dark. Figure adapted from Ref. [69].

3.3 Wave Function Imaging

In section 2.8.3 we described the formalism used to calculate tunneling amplitudes from correlated many-body wave functions. We will illustrate it by an application to magnetotunneling spectroscopy (MTS) of self-assembled InAs quantum dots grown by the Stranskii-Krastanov method [127, 128]. We choose this system because of recent measurements on this system [20]. The experimental method is based on capacitance-voltage (C-V) spectroscopy [15, 99, 129–132] where the energy of the quantum dot states can be shifted by an applied out of plane voltage to allow electron (or hole) to tunnel into the dots controllably. Additionally, a magnetic field B is applied in-plane. The tunneling rate can be measured and compared to the theoretical

calculations [20]. Figure 7 a) shows the theoretical results for the tunneling amplitude of holes mapped out in **k**-space for an InAs lens-shaped quantum dot with an elliptical base of 26 nm in $[1\bar{1}0]$ and 25 nm in $[110]$ direction and 3.5 nm height. The labels $nh \rightarrow mh$ describes the process of tunneling the mth hole into the dot already filled with n holes. The arrows with labels $[110]$ and $[1\bar{1}0]$ describe the crystallographic directions in real-space. From the Figure it is clear that tunneling of the first and second hole occurs into an S-like state. We can quantitatively analyze the orbital momentum character of the final state and it is indeed to more than 95% $l = 0$. The tunneling of the third and fourth holes occurs into P-like states. For the fifth hole, **4h $\rightarrow$ 5h** the situation is interesting since it is the signature of the tunneling into the D state. Indeed 82% of the final state, in which the hole tunnels, is given by a configuration with dominant D character. In Figure 7 b) we show that the filling sequence expected from the Aufbau principle would lead to a tunneling into a second P state (labelled P2 in Figure 7 b)) and not into a D-state, as given by the many-body calculation. The holes 5 and 6 therefore entirely skip the P2 shell to tunnel directly into the D-shell, in contrast to the expectation from the Aufbau principle. This result is confirmed by a side-by-side comparison of experiment and theory [20]. In Figure 7 c) we show a contour plot for the experimental MTS result for the tunneling of the first hole along with theoretical results for a dot with circular base of 25 nm diameter and for a dot with ellipsoidal base of 24x26 nm^2. The comparison of theory and experiment shows a better fit for the elongated dot. These results should illustrate the capability to draw conclusions on dot morphology, difficult to get by other means, and on unexpected many-body effects.
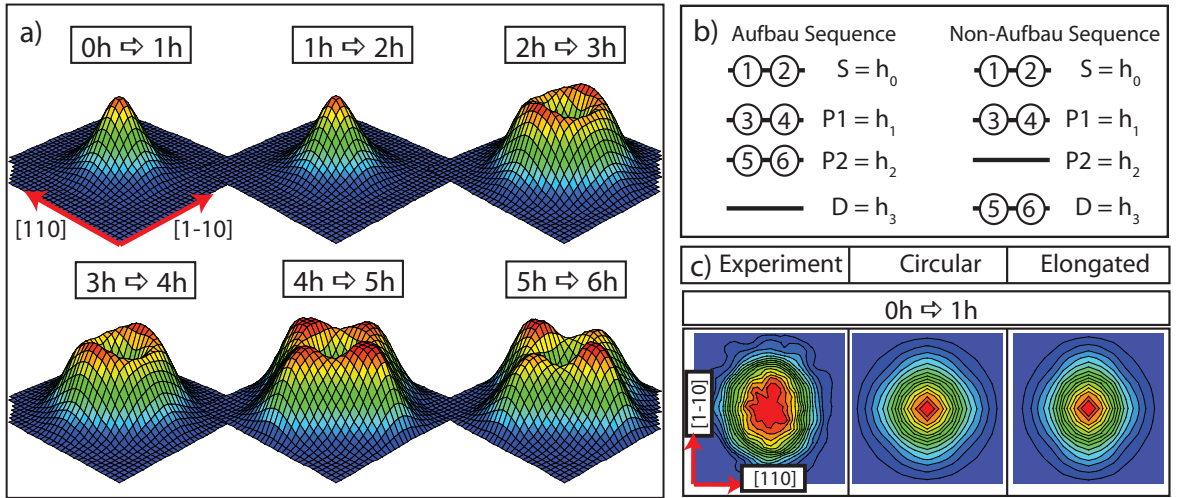
Figure 7: a) Calculated quasi-particle tunneling probability densities for 1 to 6 holes in reciprocal space [20] b) Two possible charging scenarios for holes. c) Quasi-particle tunneling probability density for the first hole from experiment (left), a calculation for a dot with circular base (middle), and a calculation for an elliptical base (right).

4   Summary and Outlook

We have described an approach to obtain accurate properties, including excitations, of semi-conductor nanostructures of realistic and relevant sizes. The approach is based on empirical or semi-empirical pseudopotentials and configuration interaction. The critical steps that allow us

to treat million atom systems are (i) we forgo the calculation of total energies and solve an inner eigenvalue problem around the band gap for a few states only, (ii) the constructed empirical potentials are total effective potentials that include the effect of valence electrons. There is no self-consistent procedure and the Hamilton matrix is solved for few eigenvalues only once. (iii) For the largest structures we use a basis set made of Bloch functions of the underlying strained bulk matrix, leading to a dense but manageable eigenvalue problem. The ensuing quasiparticle eigenfunctions can be directly used to calculate correlated few-particle states, with N electrons and M holes, by a configuration interaction treatment. This give access to observables that can be calculated using post-processor tools. The accuracy and applicability of the method was illustrated by three different applications in the area of optics, quantum entanglement and wave function imaging.

One of the appeals of the method, besides the fact that it can address a large number of atoms, may come from the fact that, for the *semi* empirical potentials, the construction is directly tied to *ab initio* methods. The results from density functional theory (DFT) are fed into the semi-empirical pseudopotentials in a controllable fashion during construction. Applications of the method are, however, seamless in the sense that no more interface between SEPM and DFT exists, unlike multi-scale approaches where this interface represents the crux of the methods. The most fundamental limitation of the method originates from one of its strength and is the lack of self-consistency. Indeed, effects related to long range charge transfer, well captured by self-consistent methods such as DFT, are absent in the SEPM framework. These effects can be sometimes included *a posteriori* as external fields, as in the case of piezoelectricity, but this represents a complication.

The solid foundation of the framework presented here, allows us to envision some interesting extensions for the coming years. A natural and useful development would be the inclusion of *dynamical processes* where electron-phonon coupling could be treated perturbatively or non-perturbatively. This would enable us to predict the effect of temperature on the observables described previously and give us access to processes forbidden in the absence of phonons, such as spin-relaxation times. These are fundamentally interesting effects, relevant to the world of technology. Another interesting avenue is the effect of magnetic fields on nanoscopic systems treated almost exclusively at continuum level until now. An accurate prediction of magnetic properties, such as g-factors, would be useful, e.g., to the area of spintronics. Yet another valuable developments would be the creation of a link between the potential construction and the modern theories beyond LDA, such as GW. Such a link could help removing some of the empirical steps in the construction and may lead to a more automatic way of pseudopotential generation, ideally close to the ones used commonly in DFT. Finally, improving the numerics and algorithms is a never ending and often surprising task that can open the way to applications and developments not easy to foresee.

References

[1] A.D. Yoffe. Semiconductor quantum dots and related systems: electronic, optical, luminescence and related properties of low dimensional systems. *Adv. Phys.*, 50:1–208, 2001.

[2] C. Celebi, P.M. Koenraad, A. Y. Silov, W. Van Roy, A. M. Monakhov, J. M. Tang, and M.E. Flatté. Anisotropic spatial structure of deep acceptor states in GaAs and gap. *Phys. Rev. B*, 77:075328, 2008.

[3] A. M. Yakunin, A. Y. Silov, P. M. Koenraad, J. M. Tang, M. E. Flatte, J. L. Primus, W. Van Roy, J. De Boeck, A. M. Monakhov, K. S. Romanov, I. E. Panaiotti, and N. S. Averkiev. Warping single Mn acceptor wavefunction by straining the GaAs host. *Nature Materials*, 6(7):512–515, Jul 2007.

[4] A. Kudelski, A. Lemaitre, A. Miard, P. Voisin, T. C. M. Graham, R. J. Warburton, and O. Krebs. Optically probing the fine structure of a single Mn atom in an InAs quantum dot. *Phys. Rev. Lett.*, 99(24):247209, Dec 2007.

[5] J. Fernandez-Rossier and L. Brey. Ferromagnetism mediated by few electrons in a semimagnetic quantum dot. *Phys. Rev. Lett.*, 93(11):117201, Sep 2004.

[6] Y. Leger, L. Besombes, L. Maingault, D. Ferrand, and H. Mariette. Geometrical effects on the optical properties of quantum dots doped with a single magnetic atom. *Phys. Rev. Lett.*, 95(4):047403, Jul 2005.

[7] L. Besombes, Y. Leger, L. Maingault, D. Ferrand, H. Mariette, and J. Cibert. Probing the spin state of a single magnetic ion in an individual quantum dot. *Phys. Rev. Lett.*, 93(20):207403, Nov 2004.

[8] Y. Leger, L. Besombes, J. Fernandez-Rossier, L. Maingault, and H. Mariette. Electrical control of a single Mn atom in a quantum dot. *Phys. Rev. Lett.*, 97(10):107401, 2006.

[9] S. C. Erwin, L. J. Zu, M. I. Haftel, A. L. Efros, T. A. Kennedy, and D. J. Norris. Doping semiconductor nanocrystals. *Nature*, 436(7047):91–94, 2005.

[10] R. J. Warburton, C. Schaflein, D. Haft, F. Bickel, A. Lorke, K. Karrai, J. M. Garcia, W. Schoenfeld, and P. M. Petroff. Optical emission from a charge-tunable quantum ring. *Nature*, 405:926, 2000.

[11] B. Urbaszek, R J Warburton, K. Karrai, B.D. Gerardot, P.M. Petroff, and J.M. Garcia. Fine structure of higly charged excitons in semiconductor quantum dots. *Phys. Rev. Lett.*, 90:247403, 2003.

[12] E Dekel, D Gershoni, E Ehrenfreund, D Spektor, J M Garcia, and P M Petroff. Multi-exciton spectroscopy of a single self-assembled quantum dot. *Phys. Rev. Lett.*, 80:4991, 1998.

[13] M Bayer, A Kuther, A Forchel, A Gorbunov, V B Timofeev, F Schäfer, J P Reithmaier, T L Reinecke, and S N Walck. Electron and hole g factors and exchange interaction from

studies of the exciton fine structure in $In_{0.60}Ga_{0.40}As$ quantum dots. *Phys. Rev. Lett.*, 82:1748, 1999.

[14] A Zrenner, F Findeis, M Baier, M Bichler, G Abstreiter, U Hohenester, and E Molinari. Optically detected single-electron charging in a quantum dot. *Physica E*, 13:95, 2002.

[15] D. Reuter, P. Kailuweit, A. D. Wieck, U. Zeitler, O. Wibbelhoff, C. Meier, A. Lorke, and J. C. Maan. Coulomb-interaction-induced incomplete shell filling in the hole system of InAs quantum dots. *Phys. Rev. Lett.*, 94:026808, 2005.

[16] L. P. Kouwenhoven, D. G. Austing, and S. Tarucha. Few-electron quantum dots. *Reports on Progress in Physics*, 64(6):701–736, 2001.

[17] D. Loss and D. P. DiVincenzo. Quantum computation with quantum dots. *Phys. Rev. A*, 57:120–126, 1998.

[18] U. Woggon. *Optical Properties of Semiconductor Quantum Dots*. Springer-Verlag, Berlin, 1997.

[19] R. D. Schaller and V. I. Klimov. High efficiency carrier multiplication in PbSe nanocrystals: Implications for solar energy conversion. *Phys. Rev. Lett.*, 92:186601, 2004.

[20] G. Bester, D. Reuter, L. He, A. Zunger, P. Kailuweit, A. D. Wieck, U. Zeitler, J. C. Maan, O. Wibbelhoff, and A. Lorke. Experimental imaging and atomistic modeling of electron and hole quasiparticle wave functions in InAs/GaAs quantum dots. *Phys. Rev. B*, 76(7):075338, Aug 2007.

[21] A. M. Yakunin, A. Y. Silov, P. M. Koenraad, J. M. Tang, M. E. Flatte, W. Van Roy, J. De Boeck, and J. H. Wolter. Spatial structure of Mn-Mn acceptor pairs in GaAs. *Phys. Rev. Lett.*, 95(25):256402, Dec 2005.

[22] D. Kitchen, A. Richardella, J. M. Tang, M. E. Flatte, and A. Yazdani. Atom-by-atom substitution of Mn in GaAs and visualization of their hole-mediated interactions. *Nature*, 442(7101):436–439, Jul 2006.

[23] G. Bastard. *Wave Mechanics Applied to Semiconductor Heterostructures*. Halstead, New York, 1988.

[24] H.X. Fu, L.-W. Wang, and A. Zunger. Applicability of the $k \cdot p$ method to the electronic structure of quantum dots. *Phys. Rev. B*, 57:9971, 1998.

[25] L.-W. Wang, A. J. Williamson, A. Zunger, H. Jiang, and J. Singh. Comparison of the k.p and direct diagonalization approaches to the electronic structure of InAs/GaAs quantum dots. *Appl. Phys. Lett.*, 76:339, 2000.

[26] G. Bester and A. Zunger. Cylindrically shaped zinc-blende semiconductor quantum dots do not have cylindrical symmetry: Atomistic symmetry, atomic relaxation, and piezoelectric effects. *Phys. Rev. B*, 71:045318, 2005.

[27] C. Delerue and M. Lannoo. *Nanostructures: theory and modelling*. Springer Verlag, Berlin and Heidelberg, 2004.

[28] G. Klimeck, F. Oyafuso, T. B. Boykin, R.C. Bowen, and P. von Allmen. Development of a nanoelectronic 3-D (NEMO 3-D) simulator for multimillion atom simulations and its application to alloyed quantum dots. *CMES-computer modeling in engineering and sciences*, 3:601, 2002.

[29] P. N. Keating. Effect of invarience requirements on the elastic strain energy of crystals with application to the diamond structure. *Phys. Rev*, 145:637–645, 1966.

[30] C Pryor, J Kim, L.-W Wang, A J.Williamson, and A. Zunger. Comparison of two methods for describing the strain profiles in quantum dots. *J. Appl. Phys.*, 83:2548, 1998.

[31] A. J. Williamson, L.-W Wang, and A. Zunger. Theoretical interpretation of the experimental electronic structure of lens-shaped self-assembled InAs/GaAs quantum dots. *Phys. Rev. B*, 62:12963, 2000.

[32] A J Williamson and A. Zunger. InAs quantum dots: Predicted electronic structure of free-standing versus GaAs-embedded structures. *Phys. Rev. B*, 59:15819, 1999.

[33] U. von Barth and C. D. Gelatt. Validity of the frozen-core approximation and pseudopotential theory for cohesive energy calculations. *Phys. Rev. B*, 21:2222, 1980.

[34] W. M. C. Foulkes and R. Haydock. Tight-binding models and density-functional theory. *Phys. Rev. B*, 39(17):12520, 1989.

[35] J. C. Phillips and L. Kleinman. New method for calculating wave functions in crystals and molecules. *Phys. Rev.*, 116:287, 1959.

[36] M. L. Cohen, M. L. and V. Heine. Cancellation of kinetic and potential energy in atoms, molecules, and solids. *Phys. Rev.*, 122:1821, 1961.

[37] W. C. Topp and J. J. Hopfield. Chemically motivated pseudopotential for sodium. *Phys. Rev. B*, 7:1295, 1973.

[38] M. T. Yin and M. L. Cohen. Theory of lattice-dynamical properties of solids - application to Si and Ge. *Phys. Rev. B*, 26:3259, 1982.

[39] E. L. Shirley, D. C. Allan, R. M. Martin, and J. D. Joannopoulos. Extended norm-conserving pseudopotentials. *Phys. Rev. B*, 40:3652, 1989.

[40] D. R. Hamann, M. Schlüter, and L. Chiang. Norm-conserving pseudopotentials. *Phys. Rev. Lett.*, 43:1494, 1979.

[41] D. Vanderbilt. Optimally smooth norm-conserving pseudopotentials. *Phys. Rev. B*, 32:8412, 1985.

[42] G. B. Bachelet, D. R. Hamann, and M. Schlüter. Pseudopotentials that work: From H to Pu. *Phys. Rev. B*, 26:4199, 1982.

[43] N. Troullier and J. L. Martins. A straightforward method for generating soft transferable pseudopotentials. *Solid State Comm.*, 74:613, 1990.

[44] G. P. Kerker. Non-singular atomic pseudopotentials for solid-state applications. *J. Phys. C: Solid St. Phys.*, 13:L189, 1980.

[45] D. Vanderbilt. Soft self-consistent pseudopotentials in a generalized eigenvalue formalism. *Phys. Rev. B*, 41:7892, 1990.

[46] P. E. Blöchl. Generalized separable potentials for electronic-structure calculations. *Phys. Rev. B*, 41:5414, 1990.

[47] P. E. Blöchl. Projector augmented-wave method. *Phys. Rev. B*, 50:17953, 1994.

[48] M. L. Cohen and V. Heine. *The fitting of pseudopotentials to experimental data and their subsequent application*, volume 24 of *Solid State Physics*. Academic Press, New York, 1970.

[49] D. Brust, J. C.. Phillips, and M. L. Cohen. Reflectance and photoemission from Si. *Phys. Rev. Lett.*, 9:389, 1962.

[50] D. Brust, F. Bassani, and J. C. Phillips. Critical points and ultraviolet reflectivity of semiconductors. *Phys. Rev. Lett.*, 9(3):94, 1962.

[51] M. L. Cohen and T. K. Bergstresser. Band structures and pseudopotential form factors for 14 semiconductors of diamond and zinc-blende structures. *Phys. Rev.*, 141(2):789, 1966.

[52] L.-W. Wang and A. Zunger. Electronic-structure pseudopotential calculations of large (approximate-to-1000 atoms) Si quantum dots. *J. Phys. Chem.*, 98(8):2158, 1994.

[53] K. A. Mäder and A. Zunger. Empirical atomic pseudopotentials for AlAs/GaAs superlattices, alloys, and nanostructures. *Phys. Rev. B*, 50:17393, 1994.

[54] Weisz G. Band structure and Fermi surface of white tin. *Phys. Rev.*, 149:504, 1966.

[55] M.S. Hybertsen and S. G. Louie. Spin-orbit splitting in semiconductors and insulators from the ab initio pseudopotential. *Phys. Rev. B*, 34:2920, 1096.

[56] G. Bester and A. Zunger. Compositional and size-dependent spectroscopic shifts in charged self-assembled $In_xGa_{1-x}As$/GaAs quantum dots. *Phys. Rev. B*, 68:073309, 2003.

[57] L. Bellaiche. *Progress in Semiconductor Materials for Optoelectronic Applications*, volume 692, pages 9–20. Mater. Res. Soc. Proc., Pittsburgh, 2002.

[58] L. Bellaiche, S.H. Wei, and A. Zunger. Localization and percolation in semiconductor alloys: GaAsN vs GaAsP. *Phys. Rev. B*, 54:17568, 1996.

[59] J. R. Chelikovsky and M. L. Cohen. Nonlocal pseudopotential calculations for the electronic structure of eleven diamond and zinc-blende semiconductors. *Phys. Rev. B*, 14:556, 1976.

[60] L.-W. Wang and A. Zunger. Local-density-derived semiempirical pseudopotentials. *Phys. Rev. B*, 51:17398, 1995.

[61] H.X. Fu, L.-W. Wang, and A. Zunger. Comparison of the k.p and the direct diagonalization approaches for describing the electronic structure of quantum dots. *Appl. Phys. Lett.*, 71:3433, 1997.

[62] L. Kleinman and D. M. Bylander. Efficacious form for model pseudopotentials. *Phys. Rev. Lett.*, 48:1425, 1982.

[63] A. Zunger, A. Franceschetti, G. Bester, W.B. Jones, K. Kim, P.A. Graf, A. Canning L-W Wang, O. Marques, C. Voemel, J. Dongarra, J. Langou, and S. Tomov. Predicting the electronic properties of 3D, million-atom semiconductor nanostructure architectures. *J. Phys.: Conf. Ser.*, 46:292, 2006.

[64] L.-W. Wang and A. Zunger. Solving Schrödingers equation around a desired energy - application to silicon quantum dots. *J. Chem. Phys.*, 100:2394, 1994.

[65] A. V. Knyazev. Toward the optimal preconditioned eigensolver: Locally optimal block preconditioned conjugate gradient method for tight-binding parametrization: Application to silicon nanostructures. *SIAM J. Sci. Comput*, 23:517, 2001.

[66] A. Stathopoulos and J.R. McCombs. A parallel, block, Jacobi-Davidson implementation for solving large eigenproblems on coarse grain environments. *Proceedings of the International Conference on Parallel and Distributed Processing, Techniques and Applications*, page 2920, 1999.

[67] L.-W Wang and A. Zunger. Linear combination of bulk bands method for large-scale electronic structure calculations on strained nanostructures. *Phys. Rev. B*, 59:15806, 1999.

[68] D.C. Sorensen, R.B. Lehoucq, C. Yang, and K. Maschhoff. ARPACK software package. Rice University, 2001.

[69] G. Bester and A. Zunger. Electric field control and optical signature of entanglement in quantum dot molecules. *Phys. Rev B*, 72(16):165334, 2005.

[70] G. A. Narvaez, G. Bester, and A. Zunger. Pressure effects on neutral and charged excitons in self-assembled (In,Ga)As/GaAs quantum dots. *Phys. Rev. B*, 72(4):041307, 2005.

[71] G. Bester, X. Wu, D. Vanderbilt, and A. Zunger. Importance of second-order piezoelectric effects in zinc-blende semiconductors. *Phys. Rev. Lett.*, 96:187602, 2006.

[72] G. Bester, A. Zunger, X. Wu, and D. Vanderbilt. Effects of linear and nonlinear piezoelectricity on the electronic properties of InAs/GaAs quantum dots. *Phys. Rev. B*, 74:081305(R), 2006.

[73] A. Szabo and N. S. Ostlund. *Modern Quantum Chemistry*. McGraw-Hill, New York, 1989.

[74] A. Franceschetti, H Fu, L.-W Wang, and A. Zunger. Many-body pseudopotential theory of excitons in InP and CdSe quantum dots. *Phys. Rev. B*, 60:1819, 1999.

[75] L. X. Benedict. Screening in the exchange term of the electron-hole interaction of the Bethe-Salpeter equation. *Phys. Rev. B*, 66:193105, 2002.

[76] G. Bester, S. Nair, and A. Zunger. Pseudopotential calculation of the excitonic fine structure of million-atom self-assembled $In_{1-x}Ga_xAs/GaAs$ quantum dots. *Phys. Rev. B*, 67:R161306, 2003.

[77] R. Resta. Thomas-Fermi dielectric screening in semiconductors. *Phys. Rev. B*, 16:2717, 1977.

[78] H. Haken. Kopplung nichtrelativistischer Teilchen mit einem quantisierten Feld .1. das Exziton im schwingenden, polaren Kristall. *Nuovo Cimento*, 3:1230, 1956.

[79] C. Delerue, M. Lannoo, and G. Allan. Concept of dielectric constant for nanosized systems. *Phys. Rev. B*, 68(11):115411, 2003.

[80] X. Cartoixa and L.-W. Wang. Microscopic dielectric response functions in semiconductor quantum dots. *Phys. Rev. Lett.*, 94(23):236804, 2005.

[81] L.E. Brus. A simple-model for the ionization-potential, electron-affinity, and aqueous redox potentials of small semiconductor crystallites. *J. Chem. Phys.*, 79(11):5566, 1983.

[82] L.E. Brus. Electron electron and electron-hole interactions in small semiconductor crystallites - the size dependence of the lowest excited electronic state. *J. Chem. Phys.*, 80(9):4403, 1984.

[83] A. Franceschetti and A. Zunger. Hund's rule, spin blockade, and the aufbau principle in strongly confined semiconductor quantum dots. *Europhys. Lett.*, 50:243, 2000.

[84] L.-W. Wang. Charging effects in a CdSe nanotetrapod. *J. Phys. Chem. B*, 109(49):23330, 2005.

[85] A. Franceschetti, L.-W. Wang, G. Bester, and A. Zunger. Confinement-induced versus correlation-induced electron localization and wave function entanglement in semiconductor nano dumbbells. *Nano Lett.*, 6:1069, 2006.

[86] L. Hedin. New method for calculating 1-particle greens function with application to electron-gas problem. *Phys. Rev.*, 139(3A):A796–+, 1965.

[87] P.Y. Yu and M. Cardona. *Fundamentals of Semiconductors*. Springer, Berlin, 2001.

[88] G. A. Narvaez, G. Bester, and A. Zunger. Excitons, biexcitons, and trions in self-assembled (In,Ga)As/GaAs quantum dots: Recombination energies, polarization, and radiative lifetimes versus dot height. *Phys. Rev. B*, 72(24):245318, 2005.

[89] A. Thranhardt, C. Ell, G. Khitrova, and H. M. Gibbs. Relation between dipole moment and radiative lifetime in interface fluctuation quantum dots. *Phys. Rev. B*, 65(3):035327, 2002.

[90] E. Dekel, D. V. Regelman, D. Gershoni, E. Ehrenfreund, W. V. Schoenfeld, and P. M. Petroff. Cascade evolution and radiative recombination of quantum dot multiexcitons studied by time-resolved spectroscopy. *Phys. Rev. B*, 62:11038, 2000.

[91] M. A. Nielsen and I. L. Chuang. *Quantum Computation and Quantum Information*. Cambridge University Press, Cambridge, 2000.

[92] C. H. Bennett, H. J. Bernstein, S. Popescu, and B. Schumacher. Concentrating partial entanglement by local operations. *Phys. Rev. A*, 53:2046, 1996.

[93] G. Bester, J. Shumway, and A. Zunger. Theory of excitonic spectra and entanglement engineering in dot molecules. *Phys. Rev. Lett.*, 93:47401, 2004.

[94] L. X. He, G. Bester, and A. Zunger. Electronic asymmetry in self-assembled quantum dot molecules made of identical InAs/GaAs quantum dots. *Phys. Rev. B*, 72(8):081311, 2005.

[95] L. X. He, G. Bester, and A. Zunger. Singlet-triplet splitting, correlation, and entanglement of two electrons in quantum dot molecules. *Phys. Rev. B*, 72(19):195307, 2005.

[96] C.N. Yang. Concept of off-diagonal long-range order and quantum phases of liquid He and of superconductors. *Rev. Mod. Phys.*, 34:694, 1962.

[97] J. Schliemann, J. I. Cirac, M. Kus, M. Lewenstein, and D. Loss. Quantum correlations in two-fermion systems. *Phys. Rev. A*, 64:022303, 2001.

[98] J. Bardeen. Tunnelling from a many-particle point of view. *Phys. Rev. Lett.*, 6:57, 1961.

[99] M. Rontani and E. Molinari. Imaging quasiparticle wave functions in quantum dots via tunneling spectroscopy. *Phys. Rev. B*, 71(23):233106, 2005.

[100] L. X. He, G. Bester, Z. Q. Su, and A. Zunger. Calculation of near-field scanning optical images of exciton, charged-exciton, and multiexciton wave functions in self-assembled InAs/GaAs quantum dots. *Phys. Rev. B*, 76(3):035313, Jul 2007.

[101] G. Bester, A. Zunger, and J. Shumway. Broken-symmetry and quantum entanglement of an exciton in InGaAs/GaAs quantum dot molecules. *Phys. Rev. B*, 71:075325, 2005.

[102] L. He, G. Bester, and A. Zunger. Strain-induced interfacial hole localization in self-assembled quantum dots: Compressive InAs/GaAs versus tensile InAs/InSb. *Phys. Rev. B*, 70:235316, 2004.

[103] G. A. Narvaez, G. Bester, and A. Zunger. Dependence of the electronic structure of self-assembled (In,Ga)As/GaAs quantum dots on height and composition. *J. Appl. Phys.*, 98(4):043708, 2005.

[104] G. A. Narvaez, L He, G. Bester, and A. Zunger. Theoretical predictions of the electronic and optical properties of single and coupled (In,Ga)As/GaAs quantum dots. *Phys. E*, 32:93, 2006.

[105] L.-W. Wang and A. Zunger. Pseudopotential calculations of nanoscale CdSe quantum dots. *Phys. Rev. B*, 53(15):9579–9582, 1996.

[106] L.-W. Wang and A. Zunger. High-energy excitonic transitions in CdSe quantum dots. *J. Phys. Chem. B*, 102(34):6449–6454, 1998.

[107] L.-W. Wang, M. Califano, A. Zunger, and A Franceschetti. Pseudopotential theory of Auger processes in CdSe quantum dots. *Phys. Rev. Lett.*, 91(5), 2003.

[108] A Franceschetti and A. Zunger. Addition energies and quasiparticle gap of CdSe nanocrystals. *Appl. Phys. Lett.*, 76(13):1731–1733, 2000.

[109] M. Califano, A. Zunger, and A. Franceschetti. Direct carrier multiplication due to inverse auger scattering in CdSe quantum dots. *Appl. Phys. Lett.*, 84:2409, 2004.

[110] M. Califano, A. Franceschetti, and A. Zunger. Lifetime and polarization of the radiative decay of excitons, biexcitons, and trions in CdSe nanocrystal quantum dots. *Phys. Rev. B*, 75(11), 2007.

[111] L. He, G. Bester, and A. Zunger. Prediction of an excitonic ground state in InAs/InSb quantum dots. *Phys. Rev. Lett.*, 94:016801, 2005.

[112] J. M. An, A. Franceschetti, S. V. Dudiy, and A. Zunger. The peculiar electronic structure of PbSe quantum dots. *Nano Lett.*, 6(12):2728–2735, 2006.

[113] A. Franceschetti, J. M. An, and A. Zunger. Impact ionization can explain carrier multiplication in PbSe quantum dots quantum dots. *Nano Lett.*, 6:2191, 2006.

[114] M. Gong, K. D., C.-F. Li, R. Magri, G. A. Narvaez, and L. He. Electronic structure of self-assembled InAs/InP quantum dots: Comparison with self-assembled InAs/GaAs quantum dots. *Phys. Rev. B*, 77:045326, 2008.

[115] P. R. C. Kent and A. Zunger. Theory of electronic structure evolution in GaAsN and GaPN alloys. *Phys. Rev. B*, 6411(11), 2001. 115208.

[116] M. Ediger, G. Bester, B. D. Gerardot, A. Badolato, P. M. Petroff, K. Karrai, A. Zunger, and R. J. Warburton. Fine structure of negatively and positively charged excitons in semiconductor quantum dots: Electron-hole asymmetry. *Phys. Rev. Lett.*, 98:036808, 2007.

[117] M. Ediger, G. Bester, A. Badolato, P. M. Petroff, K. Karrai, A. Zunger, and R. J. Warburton. Peculiar many-body effects revealed in the spectroscopy of highly charged quantum dots. *Nature Physics*, 3(11):774–779, Nov 2007.

[118] M. Pi, A. Emperador, M. Barranco, F. Garcias, K. Muraki, S. Tarucha, and D. G. Austing. Dissociation of vertical semiconductor diatomic artificial molecules. *Phys. Rev. Lett.*, 87:066801, 2001.

[119] M. Rontani, S. Amaha, K. Muraki, F. Manghi, E. Molinari, S. Tarucha, and D. G. Austing. Molecular phases in coupled quantum dots. *Phys. Rev. B*, 69:085327, 2004.

[120] F. R. Waugh, M. J. Berry, D. J. Mar, R. M. Westervelt, K. L. Campman, and A. C. Gossard. Single-electron charging in double and triple quantum dots with tunable coupling. *Phys. Rev. Lett.*, 75:705, 1995.

[121] M. Bayer, P. Hawrylak, K. Hinzer, S. Fafard, M. Korkusinski, Z. R. Wasilewski, O. Stern, and A. Forchel. Coupling and entangling of quantum states in quantum dot molecules. *Science*, 291:451–453, 2001.

[122] P. W. Fry, I. E. Itskevich, D. J. Mowbray, M. S. Skolnick, J. J. Finley, J. A. Barker, E. P. O'Reilly, L. R. Wilson, I. A. Larkin, P. A. Maksym, M. Hopkinson, Al.-M. Khafaji, J. P. R. David, A. G. Cullis, G. Hill, and J. C. Clark. Inverted electron-hole alignment in InAs-GaAs self-assembled quantum dots. *Phys. Rev. Lett.*, 84:733, 2000.

[123] M. Sugisaki, H. W. Ren, S. V. Nair, K. Nishi, and Y. Masumoto. External-field effects on the optical spectra of self-assembled InP quantum dots. *Phys. Rev. B*, 66(23):235309, 2002.

[124] B. Alen, F. Bickel, K. Karrai, R.J. Warburton, and P.M. Petroff. Stark-shift modulation absorption spectroscopy of single quantum dots. *Appl. Phys. Lett.*, 83(11):2235, 2003.

[125] H. J. Krenner, M. Sabathil, E. C. Clark, A. Kress, D. Schuh, M. Bichler, G. Abstreiter, and J. J. Finley. Direct observation of controlled coupling in an individual quantum dot molecule. *Phys. Rev. Lett.*, 94:057402, 2005.

[126] G. Ortner, M. Bayer, Y. Lyanda-Geller, T. L. Reinecke, A. Kress, J. P. Reithmaier, and A. Forchel. Control of vertically coupled InGaAs/GaAs quantum dots with electric fields. *Phys. Rev. Lett.*, 94:157401, 2005.

[127] S. Guha, A. Madhukar, and K. C. Rajkumar. Onset of incoherency and defect introduction in the initial-stages of molecular-beam epitaxial-growth of highly strained $In_xGa_{1-x}As$ on GaAs(100). *Appl. Phys. Lett.*, 57:2110, 1990.

[128] D. Bimberg, M. Grundmann, and N. N. Ledentsov. *Quantum Dot Heterostructures*. John Wiley & Sons, New York, 1999.

[129] H. Drexler, D. Leonard, W. Hansen, J. P. Kotthaus, and P. M. Petroff. Spectroscopy of quantum levels in charge-tunable InGaAs quantum dots. *Phys. Rev. Lett.*, 73:2252, 1994.

[130] M. Fricke, A. Lorke, J. P. Kotthaus, G. MedeirosRibeiro, and P. M. Petroff. Shell structure and electron-electron interaction in self-assembled InAs quantum dots. *Europhys. Lett.*, 36(3):197–202, 1996.

[131] A. Patane, R. J. A. Hill, L. Eaves, P. C. Main, M. Henini, M. L. Zambrano, A. Levin, N. Mori, C. Hamaguchi, Y. V. Dubrovskii, E. E. Vdovin, D. G. Austing, S. Tarucha, and G. Hill. Probing the quantum states of self-assembled InAs dots by magnetotunneling spectroscopy. *Phys. Rev. B*, 65(16):165308, 2002.

[132] E. E. Vdovin, A. Levin, A. Patane, L. Eaves, P. C. Main, Y. N. Khanin, Y. V. Dubrovskii, M. Henini, and G. Hill. Imaging the electron wave function in self-assembled quantum dots. *Science*, 290(5489):122–124, 2000.

[133] A. M. Stoneham and J. L. Gavartin. Dynamics at the nanoscale. *Materials Science & Engineering C*, 27(5-8):972–980, 2007.